Two-dimensional optical spectroscopy of excitons in semiconductor quantum wells: Liouville-space pathway analysis

Lijun Yang,[1] Igor V. Schweigert,[1] Steven T. Cundiff,[2] and Shaul Mukamel[1]

[1]*Chemistry Department, University of California, Irvine, California, 92697-2025, USA*
[2]*JILA, University of Colorado and National Institute of Standards and Technology, Boulder, Colorado 80309-0440, USA*

We demonstrate how dynamic correlations of heavy-hole and light-hole excitons in semiconductor quantum wells may be investigated by two-dimensional correlation spectroscopy. The coherent response to three femtosecond optical pulses is predicted to yield cross (off-diagonal) peaks that contain direct signatures of many-body two-exciton correlations. Signals generated at various phase-matching directions are compared.

I. INTRODUCTION

Understanding the signatures of many-body interactions in the nonlinear optical response of semiconductors is an important fundamental problem with implications to all-optical and electro-optical device applications.[1] The linear response to a weak optical field is well described by a model of noninteracting quasiparticles. However, residual interactions, not accounted for by these quasiparticles, can considerably affect the nonlinear response. Similar to Frenkel excitons in molecular crystals and aggregates,[2] Coulomb correlations among quasiparticles can dominate the nonlinear optical response of semiconductors, in marked contrast to the behavior of atomic systems.[3–13]

The coherent ultrafast response and many-body correlations in semiconductor heterostructures have been studied extensively in the past two decades.[5,14–25] Due to various dephasing and relaxation mechanisms, the coherent response usually persists only on the tens of picosecond time scale. Optical spectra such as the linear absorption, pump-probe and four-wave mixing (FWM) are commonly displayed as a function of a single (time or frequency) variable and hence provide a one-dimensional (1D) projection of the microscopic information. One-dimensional spectra are hard to interpret in systems with many congested energy levels. The spectroscopic signatures of complex many-body dynamics projected on a 1D spectral plot strongly overlap and may not be easily identified. For example, when 1D techniques are employed in III-V semiconductor quantum wells (QWs), it is difficult to pinpoint the signatures of two-excitons due to the small (1–2 meV) two-exciton interaction energies, i.e., bound two-exciton binding energy and unbound two-exciton scattering energy.[26–28] Two-exciton effects can be easily masked by homogeneous and inhomogeneous line broadenings. When both light-hole (LH) and heavy-hole (HH) excitons and their interactions are taken into account, the situation becomes even more complicated since there are different types of two-excitons such as LH, HH, and mixed two-excitons.[28,29] Even in II-VI semiconductor QWs, where the two-exciton interaction energies are much larger (from several to several tens of meV),[29] it is still hard to resolve them.

Multidimensional spectroscopy,[2,30–35] in which the optical response is recorded and displayed versus several arguments, can overcome these limitations by separating the signatures of different pathways of the density matrix, known as the Liouville-space pathways.[36] Because different pathways are usually connected with specific couplings, one can resolve different coherences and many-body interactions by focusing on different peaks in multidimensional correlation plots. Optical and infrared two-dimensional correlation spectroscopy (2DCS) is a femtosecond analog of multidimensional nuclear magnetic resonance[37,38] (NMR) that has been shown to be very powerful for probing the structure and dynamics in chemical and biological systems.[35,39–45] These techniques can reveal the coupling strength of elementary excitations through *cross peaks*. After several attempts[46–50] to go beyond 1D techniques, an experimental implementation of 2DCS to investigate the many-body Coulomb interactions among LH and HH excitons in semiconductors has been reported recently.[51,52]

In this work, we present the basic principles[2,34] of 2DCS in semiconductor QWs and show how it can be used to study the couplings among LH and HH excitons in a GaAs single quantum well. The same methodology previously applied to Frenkel excitons (hard-core bosons) in molecular aggregates or anharmonic vibrations (soft-core bosons) in proteins[2,34] can be extended to Wannier excitons.[31,32,53,54] In Sec. II, we survey the possible third-order 2D techniques of excitons. The double-sided Feynman diagrams and the corresponding sum-over-states expressions for 2DCS in III-V semiconductor quantum wells are presented in Sec. III. These guide the analysis of the numerical calculations presented in later sections. In Sec. IV, we present the multiband Hamiltonian and the nonlinear exciton equations used for the numerical calculation of the 2DCS signals. The numerical calculations are analyzed in Sec. V. Finally, in Sec. VI, we summarize our findings.

II. LIOUVILLE-SPACE PATHWAY ANALYSIS FOR 2D CORRELATION SPECTROSCOPY OF EXCITONS

Impulsive 2DCS signals generated by well-separated femtosecond pulses may be calculated using sum-over-states expressions, which provide insights into the origin of various peaks associated with different coherences and many-body interactions. These expressions will be used in the following sections to analyze the 2D signals obtained by numerical solution of equations of motion with finite-envelope pulses.

We consider a three-pulse sequence where the electric field is given by

$$\mathbf{E}(\mathbf{r},t) = \sum_{j=1}^{3} [\mathbf{e}_j \mathcal{E}_j^+(t-\tau_j)e^{i(\mathbf{k}_j \cdot \mathbf{r}-\omega_j t)} + \mathbf{e}_j \mathcal{E}_j^-(t-\tau_j)e^{-i(\mathbf{k}_j \cdot \mathbf{r}-\omega_j t)}].$$

$$(1)$$

Here, $\mathcal{E}_j^+$ $[\mathcal{E}_j^- = (\mathcal{E}_j^+)^*]$ is the envelope of the positive (negative)-frequency component of the jth pulse centered at τ_j, with carrier frequency ω_j, polarization unit vector $\mathbf{e}_j$, and wave vector $\mathbf{k}_j$. The ability to vary the envelopes, polarization directions, durations, and time intervals tune the frequencies and even control the phases of optical pulses, provides a broad class of possible techniques. By scanning these various parameters, it is possible to design a multiple-pulse technique[2,34] for a specific application, as is done in NMR.[55]

The total Hamiltonian is

$$H = H_0 - \mu \cdot E(\mathbf{r},t),$$

where H_0 is the free system Hamiltonian and μ is the dipole operator. The third-order contribution to the system's polarization induced by the interaction with the field can be written as

$$P_{e_4}(\mathbf{r},t) = \int_0^\infty \int_0^\infty \int_0^\infty dt_1 dt_2 dt_3 R^{(3)}_{e_4 e_3 e_2 e_1}(t_3,t_2,t_1) E_{e_3}$$

$$\times (\mathbf{r}, t-t_3) E_{e_2}(\mathbf{r}, t-t_3-t_2) E_{e_1}(\mathbf{r}, t-t_3-t_2-t_1).$$

$$(2)$$

Here, $R^{(3)}$ is the third-order response function calculated using time-dependent perturbation theory,

$$R^{(3)}_{e_4 e_3 e_2 e_1}(t_3,t_2,t_1)$$

$$= i^3 \langle [[[\hat{\mu}_{e_4}(t),$$

$$\hat{\mu}_{e_3}(t-t_3)], \hat{\mu}_{e_2}(t-t_3-t_2)], \hat{\mu}_{e_1}(t-t_3-t_2-t_1)]\rangle, \quad (3)$$

where $\hat{\mu}_{e_j}(t)$ are interaction picture operators. $R^{(3)}$ is a tensor of rank 4, but for clarity, we hereafter suppress the tensor indices e_j. In impulsive experiments where the field envelopes are much shorter than the delay periods and the exciton dynamics time scale, the system first interacts with the $\mathbf{k}_1$ pulse, then with $\mathbf{k}_2$, and finally with $\mathbf{k}_3$, and the time integrations in Eq. (2) can be eliminated. We then get

$$P^{(3)}(\mathbf{r},t) = R^{(3)}(t_3,t_2,t_1)\mathcal{E}_3^\pm \mathcal{E}_2^\pm \mathcal{E}_1^\pm e^{i(\pm\mathbf{k}_1 \pm \mathbf{k}_2 \pm \mathbf{k}_3)\mathbf{r}} e^{-i(\pm\omega_1 \pm \omega_2 \pm \omega_3)t}$$

$$\times e^{i(\pm\omega_1 \pm \omega_2 \pm \omega_3)t_3} e^{i(\pm\omega_1 \pm \omega_2)t_2} e^{\pm i\omega_1 t_1}.$$

We shall recast the polarization in the form

$$P^{(3)}(\mathbf{r},t) = \sum_s P_s(t_3,t_2,t_1)e^{i\mathbf{k}_s \mathbf{r} - i\omega_s t} + \text{c.c.}, \quad (4)$$

where the signal wave vector $\mathbf{k}_s$ can assume one of the four phase-matching values: $\mathbf{k}_I = -\mathbf{k}_1 + \mathbf{k}_2 + \mathbf{k}_3$, $\mathbf{k}_{II} = \mathbf{k}_1 - \mathbf{k}_2 + \mathbf{k}_3$, $\mathbf{k}_{III} = \mathbf{k}_1 + \mathbf{k}_2 - \mathbf{k}_3$, and $\mathbf{k}_{IV} = \mathbf{k}_1 + \mathbf{k}_2 + \mathbf{k}_3$.

By employing heterodyne detection and controlling the relative phases of the heterodyne and incident fields, one can detect the signal field itself (both amplitude and phase) rather
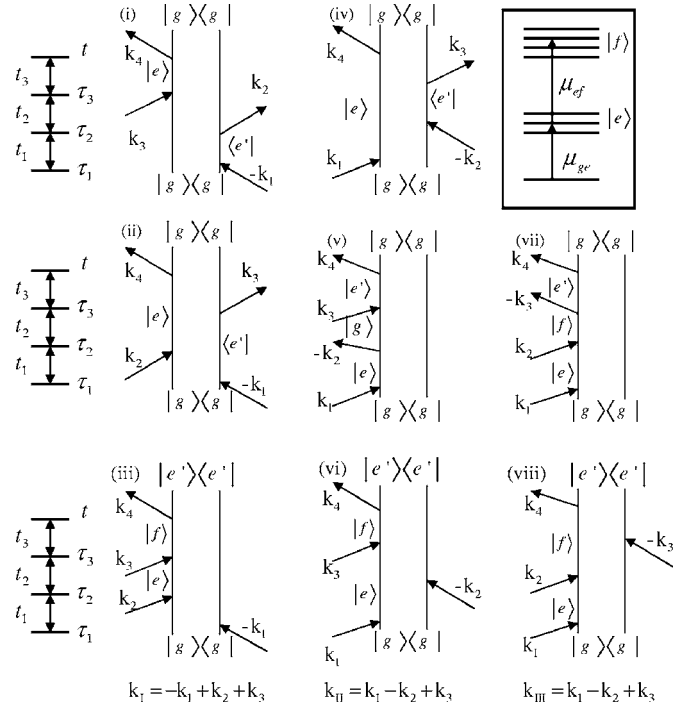

FIG. 1. Feynman diagrams for the possible coherent 2D spectroscopic techniques for the exciton level scheme given in the top right. $|g\rangle$ is the ground state, $|e\rangle$ is the single-exciton manifold, and $|f\rangle$ is the two-exciton manifold. μ_{ge} and μ_{ef} are the corresponding transition dipoles (from Ref. 2).

than merely its intensity (modulus square). In thin samples, propagation effects are negligible and the signal field is proportional to the polarization field. Hereafter, we denote the signal field amplitudes generated along $\mathbf{k}_j$ as $\mathbf{S}_j$, where $j=$ I, II, III, and IV. These are given by

$$S_I(t_3,t_2,t_1) = iR_I^{(3)}(t_3,t_2,t_1)\mathcal{E}_3^+ \mathcal{E}_2^+ \mathcal{E}_1^- e^{i(-\omega_1+\omega_2+\omega_3)t_3}$$

$$\times e^{i(-\omega_1+\omega_2)t_2}e^{-i\omega_1 t_1}, \quad (5)$$

$$S_{II}(t_3,t_2,t_1) = iR_{II}^{(3)}(t_3,t_2,t_1)\mathcal{E}_3^+ \mathcal{E}_2^- \mathcal{E}_1^+ e^{i(\omega_1-\omega_2+\omega_3)t_3}e^{i(\omega_1-\omega_2)t_2}e^{i\omega_1 t_1},$$

$$(6)$$

$$S_{III}(t_3,t_2,t_1) = iR_{III}^{(3)}(t_3,t_2,t_1)\mathcal{E}_3^- \mathcal{E}_2^+ \mathcal{E}_1^+ e^{i(\omega_1+\omega_2-\omega_3)t_3}e^{i(\omega_1+\omega_2)t_2}e^{i\omega_1 t_1},$$

$$(7)$$

$$S_{IV}(t_3,t_2,t_1) = iR_{IV}^{(3)}(t_3,t_2,t_1)\mathcal{E}_3^+ \mathcal{E}_2^+ \mathcal{E}_1^+ e^{i(\omega_1+\omega_2+\omega_3)t_3}e^{i(\omega_1+\omega_2)t_2}e^{i\omega_1 t_1}.$$

$$(8)$$

The exciton level scheme[2,34] for the two-band model of semiconductor shown in Fig. 1 (top right) consists of three manifolds: the ground state (g), single-exciton states (e), and two-exciton states (f). The dipole operator only connects the g to e and e to f manifolds. Within the rotating wave approximation (RWA), $R_{IV}^{(3)}$ vanishes for this model, and the response functions $R_j^{(3)}$ [Eqs. (5)–(7)] for the other techniques are represented by the double-sided Feynman diagrams[2,36] shown in Fig. 1.

The sum-over-states expression for $R_I^{(3)}$ is

$$R_I^{(3)}(t_3,t_2,t_1) = i^3 \sum_{e,e'} (\mathbf{e}_1 \cdot \boldsymbol{\mu}_{ge'})(\mathbf{e}_2 \cdot \boldsymbol{\mu}_{e'g})(\mathbf{e}_4 \cdot \boldsymbol{\mu}_{ge})(\mathbf{e}_3 \cdot \boldsymbol{\mu}_{eg}) e^{-(i\omega_{eg}+\Gamma_{eg})t_3 - \Gamma_{gg}t_2 + (i\omega_{e'g}-\Gamma_{e'g})t_1}$$

$$+ i^3 \sum_{e,e'} (\mathbf{e}_1 \cdot \boldsymbol{\mu}_{ge'})(\mathbf{e}_3 \cdot \boldsymbol{\mu}_{e'g})(\mathbf{e}_4 \cdot \boldsymbol{\mu}_{ge})(\mathbf{e}_2 \cdot \boldsymbol{\mu}_{eg}) e^{-(i\omega_{eg}+\Gamma_{eg})t_3 - (i\omega_{ee'}+\Gamma_{ee'})t_2 + (i\omega_{e'g}-\Gamma_{e'g})t_1}$$

$$- i^3 \sum_{e,e',f} (\mathbf{e}_1 \cdot \boldsymbol{\mu}_{ge'})(\mathbf{e}_4 \cdot \boldsymbol{\mu}_{e'f})(\mathbf{e}_3 \cdot \boldsymbol{\mu}_{fe})(\mathbf{e}_2 \cdot \boldsymbol{\mu}_{eg}) e^{-(i\omega_{fe'}+\Gamma_{fe'})t_3 - (i\omega_{ee'}+\Gamma_{ee'})t_2 + (i\omega_{e'g}-\Gamma_{e'g})t_1}, \tag{9}$$

where $\omega_{vv'} = \varepsilon_v - \varepsilon_{v'}$ ($v, v' = g, e, e', f$) is the frequency and $\Gamma_{vv'}$ are the dephasing rate of the $v \rightarrow v'$ transition. The three terms correspond, respectively, to diagrams (i), (ii), and (iii).

The 2D signal is displayed in the frequency domain by a Fourier transform of $S_I(t_3,t_2,t_1)$ with respect to t_3 and t_1, holding t_2 fixed,

$$S_I^{(3)}(\Omega_3,t_2,\Omega_1) \equiv \int \int dt_3 dt_1 S_I(t_3,t_2,t_1) e^{i\Omega_3 t_3} e^{i\Omega_1 t_1}. \tag{10}$$

This gives

$$S_I^{(3)}(\Omega_3,t_2,\Omega_1) = \sum_{e,e'} \frac{e^{-\Gamma_{gg}t_2}(\mathbf{e}_1 \cdot \boldsymbol{\mu}_{ge'})(\mathbf{e}_2 \cdot \boldsymbol{\mu}_{e'g})(\mathbf{e}_4 \cdot \boldsymbol{\mu}_{ge})(\mathbf{e}_3 \cdot \boldsymbol{\mu}_{eg})\mathcal{E}_3^+\mathcal{E}_2^+\mathcal{E}_1^-}{[\Omega_3 - \omega_{eg} - \omega_1 + \omega_2 + \omega_3 + i\Gamma_{eg}][\Omega_1 + \omega_{e'g} - \omega_1 + i\Gamma_{e'g}]}$$

$$+ \sum_{e,e'} \frac{e^{-(i\omega_{ee'}+\Gamma_{ee'})t_2}(\mathbf{e}_1 \cdot \boldsymbol{\mu}_{ge'})(\mathbf{e}_3 \cdot \boldsymbol{\mu}_{e'g})(\mathbf{e}_4 \cdot \boldsymbol{\mu}_{ge})(\mathbf{e}_2 \cdot \boldsymbol{\mu}_{eg})\mathcal{E}_3^+\mathcal{E}_2^+\mathcal{E}_1^-}{[\Omega_3 - \omega_{eg} - \omega_1 + \omega_2 + \omega_3 + i\Gamma_{eg}][\Omega_1 + \omega_{e'g} - \omega_1 + i\Gamma_{e'g}]}$$

$$- \sum_{e,e'} \sum_f \frac{e^{-(i\omega_{ee'}+\Gamma_{ee'})t_2}(\mathbf{e}_1 \cdot \boldsymbol{\mu}_{ge'})(\mathbf{e}_4 \cdot \boldsymbol{\mu}_{e'f})(\mathbf{e}_3 \cdot \boldsymbol{\mu}_{fe})(\mathbf{e}_2 \cdot \boldsymbol{\mu}_{eg})\mathcal{E}_3^+\mathcal{E}_2^+\mathcal{E}_1^-}{[\Omega_3 - \omega_{fe'} - \omega_1 + \omega_2 + \omega_3 + i\Gamma_{fe'}][\Omega_1 + \omega_{erimeg} - \omega_1 + i\Gamma_{e'g}]}. \tag{11}$$

Equation (11) has various diagonal peaks ($\Omega_1 = \Omega_3$) and cross peaks ($\Omega_1 \neq \Omega_3$). The relative contributions of different terms may be controlled by the carrier frequencies ω_1, ω_2, and ω_3. Spreading the signal in an extra frequency dimension enhances the resolving power of the 2DCS, compared to 1D techniques.[2] We can further improve the resolution by controlling other parameters such as the pulse polarization directions, carrier frequencies, and envelopes. Other 2D techniques generated in different phase-matching directions and using different pairs of time variables (e.g., t_2 and t_3) provide complementary information[2,34,56] through different projections of the response, as will be discussed in Sec. III. Closed expressions for the other 2D signals $\mathbf{S}_{II}$ and $\mathbf{S}_{III}$ are given in Appendix A.

III. APPLICATION TO III-V SEMICONDUCTOR QUANTUM WELLS

A. Single- and two-exciton resonances

The dipole selection rules for HH and LH excitons in III-V semiconductor quantum wells are shown in Fig. 2.

For GaAs, the electron effective mass $m_e = 0.065m_0$ (m_0 is the free-electron mass), while the in-plane LH and HH masses are $m_{LH}^{\parallel} = 0.206m_0$ and $m_{HH}^{\parallel} = 0.115m_0$, respectively, and perpendicular LH and HH masses are $m_{LH}^{\perp} = 0.094m_0$ and $m_{HH}^{\perp} = 0.34m_0$, respectively. The allowed transitions near the

band edge are denoted by right (σ^+) and left (σ^-) arrows, representing right- and left-circularly polarized photons, respectively. The corresponding transition dipoles μ^{vc} are

$$\mu^{v_1c_1} = \frac{1}{\sqrt{2}}\mu_0\sigma^+ = \frac{1}{\sqrt{2}}\mu_0(\hat{\mathbf{x}} + i\hat{\mathbf{y}}), \tag{12}$$

$$\mu^{v_2c_2} = \frac{1}{\sqrt{2}}\mu_0\sigma^- = \frac{1}{\sqrt{2}}\mu_0(\hat{\mathbf{x}} - i\hat{\mathbf{y}}), \tag{13}$$
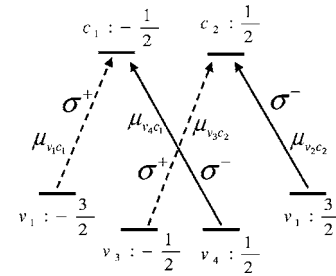
FIG. 2. Selection rules for III-V semiconductors. c_1 and c_2 are two conduction bands whose spins are $s_z = -\frac{1}{2}$ and $s_z = \frac{1}{2}$, respectively. v_1 and v_2 are HH valence bands with spins $s_z = -\frac{3}{2}$ and $s_z = \frac{3}{2}$, respectively. v_3 and v_4 are LH valence bands with spins $s_z = -\frac{1}{2}$ and $s_z = \frac{1}{2}$, respectively.
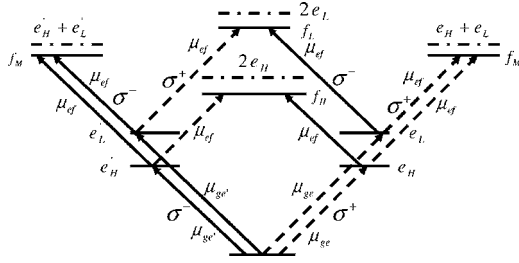
FIG. 3. Single-exciton and bound two-exciton optical transitions in III-V semiconductors.

$$\mu^{v_3 c_2} = \frac{1}{\sqrt{6}}\mu_0 \sigma^+ = \frac{1}{\sqrt{6}}\mu_0(\hat{\mathbf{x}} + i\hat{\mathbf{y}}), \tag{14}$$

$$\mu^{v_4 c_1} = \frac{1}{\sqrt{6}}\mu_0 \sigma^- = \frac{1}{\sqrt{6}}\mu_0(\hat{\mathbf{x}} - i\hat{\mathbf{y}}), \tag{15}$$

where $\hat{\mathbf{x}}$ and $\hat{\mathbf{y}}$ are unit vectors and μ_0 is the modulus of the transition dipole.

We denote each type of exciton by the (hole, electron) spin values involved in the valence to conduction-band transition. According to Fig. 2, there are two types of HH excitons, $\left(-\frac{3}{2}, -\frac{1}{2}\right)$ and $\left(\frac{3}{2}, \frac{1}{2}\right)$, and two types of LH excitons, $\left(-\frac{1}{2}, \frac{1}{2}\right)$ and $\left(\frac{1}{2}, -\frac{1}{2}\right)$. The system has ten types of two-excitons: three made of two single HH excitons are denoted by f_H, three made of two single LH excitons (f_L), and four made of one LH exciton and one HH exciton (f_M, mixed). Two electrons (two holes) belonging to different bands generate the following bound two-excitons.

(1) $\left(-\frac{3}{2}, -\frac{1}{2}\right) + \left(\frac{3}{2}, \frac{1}{2}\right)$: bound f_H,
(2) $\left(-\frac{1}{2}, \frac{1}{2}\right) + \left(\frac{1}{2}, -\frac{1}{2}\right)$: bound f_L,
(3) $\left(-\frac{3}{2}, -\frac{1}{2}\right) + \left(-\frac{1}{2}, \frac{1}{2}\right)$: bound f_M,

(4) $\left(\frac{3}{2}, \frac{1}{2}\right) + \left(\frac{1}{2}, -\frac{1}{2}\right)$: bound f_M. Other combinations produce the following unbound two-excitons:
(5) $\left(-\frac{3}{2}, -\frac{1}{2}\right) + \left(-\frac{3}{2}, -\frac{1}{2}\right)$: unbound f_H,
(6) $\left(\frac{3}{2}, \frac{1}{2}\right) + \left(\frac{3}{2}, \frac{1}{2}\right)$: unbound f_H,
(7) $\left(-\frac{1}{2}, \frac{1}{2}\right) + \left(-\frac{1}{2}, \frac{1}{2}\right)$: unbound f_L,
(8) $\left(\frac{1}{2}, -\frac{1}{2}\right) + \left(\frac{1}{2}, -\frac{1}{2}\right)$: unbound f_L.

The other possible two-excitons, $\left(-\frac{3}{2}, -\frac{1}{2}\right) + \left(\frac{1}{2}, -\frac{1}{2}\right)$ and $\left(\frac{3}{2}, \frac{1}{2}\right) + \left(-\frac{1}{2}, \frac{1}{2}\right)$, are expected to form unbound mixed two-exciton f_M because the electron motion dominates the internal motion of a two-exciton when the holes are much heavier than the electrons.

In Fig. 3, we show the level scheme that includes the single-exciton and the four bound two-exciton transitions.[29,57] The unbound transitions neglected in Fig. 3 for clarity will be included in the numerical calculations reported in Sec. V.

The exciton to two-exciton transition dipoles are collectively denoted by μ^{ef}, where e can be either $e_H(e_H')$ or $e_L(e_L')$ and f can be either f_H, f_L, or f_M. When all pulses are either σ^+ or σ^- polarized, the model of Fig. 3 reduces to two coupled two-level systems (dimer) whose 2DCS was studied in detail.[58]

B. Feynman diagrams for 2DCS

We first examine the Liouville-space pathways[2,36] for the S_I technique. Starting with diagram (i) in Fig. 1, we let the states e and e' assume all possible single-exciton states, as shown in Fig. 3. This yields the four Feynman diagrams (ia), (ib), (ic), and (id) depicted in Fig. 4.

The corresponding two-dimensional correlation spectrum is shown at the bottom of Fig. 4. The diagonal peak (ia) comes from HH excitons. (ib) is similarly a diagonal peak for LH excitons. The cross peak (ic) describes a pathway with LH excitons created during t_1 and HH excitons during t_3. (id) is a second cross peak representing HH excitons dur-
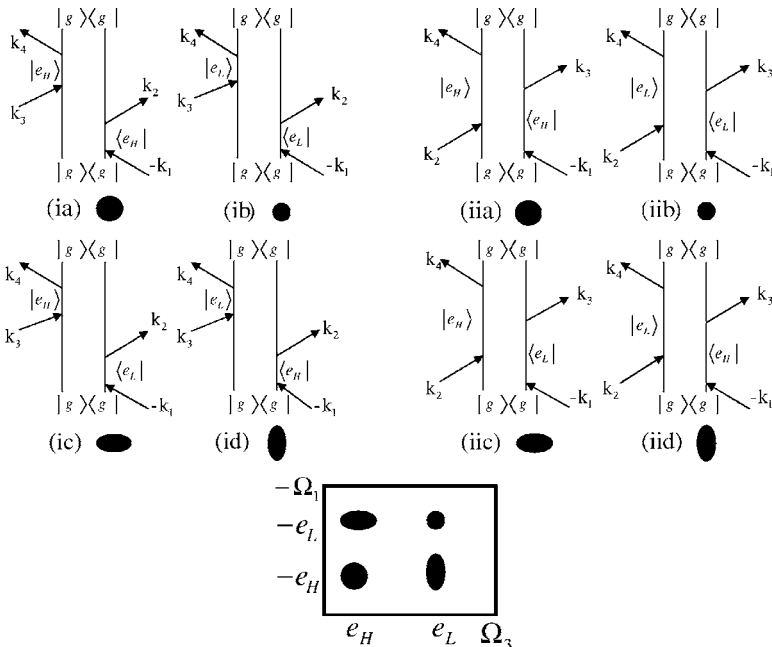

FIG. 4. Top: the Feynman diagrams derived from Fig. 1(i) and 1(ii). Bottom: the schematic 2D spectrum.
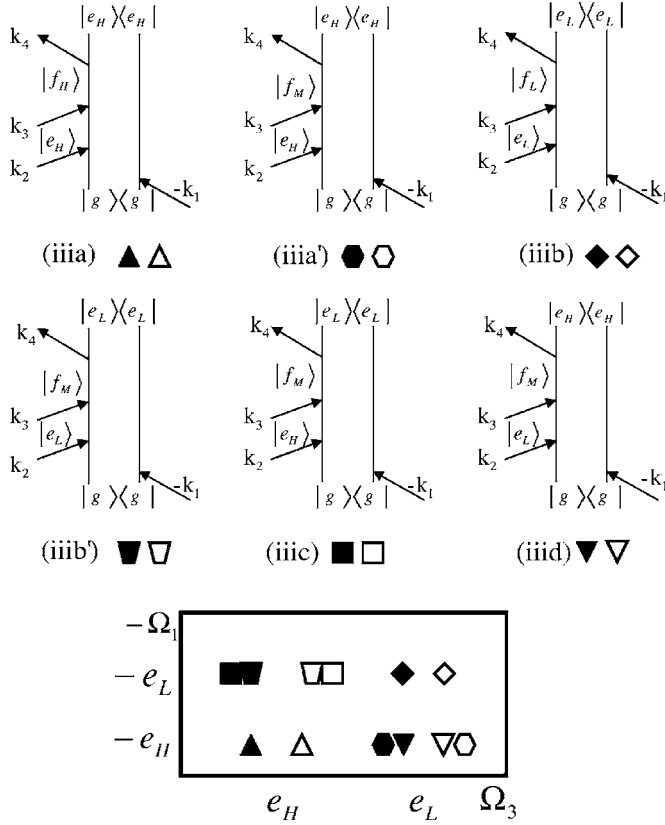
FIG. 5. Top: the Feynman diagrams derived from Fig. 1(iii). Bottom: the schematic 2D spectrum.

FIG. 6. (a) The total schematic 2D spectrum of $\mathbf{k}_I = -\mathbf{k}_1 + \mathbf{k}_2 + \mathbf{k}_3$ [diagrams (i), (ii), and (iii)]. (b) The 1DFWM signal $|\mathbf{S}_I(\Omega_3, t_2, t_1)|$ displayed vs Ω_3 for fixed t_2 and t_1.

ing t_1 and LH excitons during t_3. Diagram (ii) of Fig. 1 differs from (i) only during the t_2 period, where the system is in the excitonic rather than the ground state. Consequently, the corresponding peaks (iia), (iib), (iic), and (iid) in the (Ω_3, Ω_1) correlation plot, which show the evolution during t_1 and t_3, are the same as (ia), (ib), (ic), and (id), as shown in Fig. 4.

We next turn to diagram (iii), which involves two-exciton states. Solid (open) symbols represent bound (unbound) two-excitons which are redshifted (blueshifted) along Ω_3 with respect to the single-exciton peaks. Running the indices e, e', and f over all possible states results in the six diagrams shown Fig. 5. The corresponding 2D spectrum is shown at the bottom of Fig. 5. In the total 2D spectrum [Fig. 6(a)], which combines the spectra of Figs. 4 and 5, the two-exciton contributions (iiia)–(iiid) appear near the four single-exciton peaks of Fig. 4 (ovals and circles). There are four pathways leading to f_M, one to f_H, and one to f_L, respectively. The two-exciton peaks are either redshifted or blueshifted along Ω_3 relative to the major diagonal peaks [(e_H, $-e_H$), (e_L, $-e_L$)] or cross peaks [(e_H, $-e_L$), (e_L, $-e_H$)].

To illustrate the merits of 2DCS, we compare the 2D spectrum of Fig. 6(a) with a traditional spectrally resolved FWM (1DFWM) shown in Fig. 6(b). Using the current notation, the 1DFWM is given by $\mathbf{S}_I(\Omega_3, t_2, t_1)$, where the two pulse delays t_1 and t_2 are held fixed and Ω_3 is varied. The peak denoted by HH comes from pathways (ia), (ic), (iia), and (iic). The LH peak originates from the other four pathways (ib), (id), (iib), and (iid). In the 2D spectra [Fig. 6(a)], (iia) is separated from (iic) and (ia) is separated from (ic)
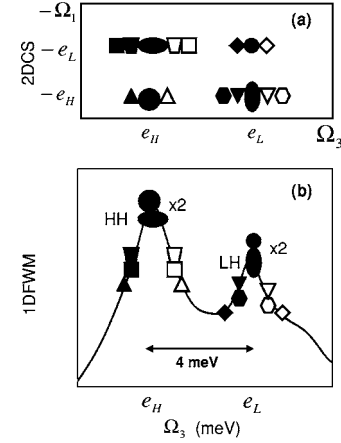
along the Ω_1 axis. We find three two-exciton contributions to the 1DFWM in Fig. 6(b) in each side of the single-exciton peak HH and three in each side of the LH peak. These contributions are very close and poorly resolved in the 1D plot because the typical two-exciton binding energies in the III-V quantum wells are 1–2 meV. Between e_H and e_L (3.8 meV for the quantum well considered), there are six types of two excitons congested in the 1D plot. In contrast, the bound mixed two-excitons (e.g., solid trapezoid and square) and bound HH two-excitons (e.g., solid triangle) are well separated along Ω_1 in the 2D plot in Fig. 6(a). Moreover, additional separation can be obtained by different projections of the $\mathbf{S}_I$ signal. For example, the overlapping mixed two-exciton contributions such as square and trapezoid in Fig. 6(a) (displaced for clarity) can be separated if we plot the 2D spectra $\mathbf{S}_I(\Omega_3, \Omega_2, t_1)$, rather than the $\mathbf{S}_I(\Omega_3, t_2, -\Omega_1)$ in Fig. 6(a) (see details in Appendix B).

To summarize this section, we have demonstrated how 2DCS can separate different pathways. In Fig. 6(a), coherences among LH and HH excitons correspond to the two major cross peaks [(e_H, $-e_L$), (e_L, $-e_H$)]], while the many-body two-exciton correlations correspond to the weak peaks around the four major peaks. Two-dimensional correlation spectroscopy with different choices of variables or along different phase-matching directions provides complementary information.

IV. HAMILTONIAN AND THE NONLINEAR EXCITON EQUATIONS

The sum-over-states expressions for 2D signals given in the previous section provide an intuitive tool for analyzing 2D techniques. Calculating the signals using these expressions requires the single-exciton and two-exciton states and their transition dipoles and relies on the impulsive-pulse assumption. This is easily done for Frenkel excitons. An alternative way to proceed, which is more practical for Wannier excitons, is to employ the nonlinear excitonic equations[34,59–62] (NEE) or the equivalent dynamics controlled truncation (DCT) formalism[5,32,63,64] to account for the

many-body interactions beyond the Hartree-Fock level.[65–79] To close the infinite hierarchy of dynamic variables, the equations of motion are truncated according to the desired order in the laser field.[5,59,60,63] Two-dimensional signals may be calculated by solving the NEE using nonequilibrium Green's functions and the two-exciton scattering matrix.[32,34,80] However, in this paper, we use direct integration of the equations of motion.

Calculating the 2DCS of semiconductor quantum wells, where excitons are spatially confined in two dimensions, requires an intensive numerical effort. Most computational work on the nonlinear optical response of two-exciton correlations focused on HH excitons. Our computation time is around 300 times higher than the corresponding 1D FWM calculation. To make these calculations more tractable, we have used a multiband one-dimensional tight-binding model[21,22,28,49,50,71,81,82] to describe the excitons and two-excitons of a single quantum well. This model can reproduce many spectroscopic observables in quantum wells such as the signs of energy shifts, bleaching, and induced absorption and often even their relative strengths and the dependence on the polarization directions of the incident pulses.[83] Comparison of the one-dimensional tight-binding with two-dimensional models can be found in Ref. 22. Other models have been successfully used as well.[20,84]

We start with the multiband tight-binding Hamiltonian[21,22,28,50,71,81,82]

$$H = H_K + H_C + H_I, \qquad (16)$$

where

$$H_K = \sum_{ijc} T_{ij}^c a_i^{c\dagger} a_j^c + \sum_{ijv} T_{ij}^v a_i^{v\dagger} a_j^v \qquad (17)$$

describes free band motion. $a_i^{c\dagger}$ (a_i^c) are creation (annihilation) Fermi operators of electrons in site i from the conduction band c and $a_i^{v\dagger}$ (a_i^v) are creation (annihilation) Fermi operators of holes in site i from the valence band v. The diagonal elements $T_{ii}^{c,v}$ describe the site energies for the electrons (holes) in the conduction (valence) band, while the off-diagonal elements $T_{i\neq j}^{c,v}$ represent the couplings between different sites. We adopt the nearest-neighbor tight-binding approximation for the electronic coupling, i.e., $T_{ij}^{c,v} = 0$ for $|i - j| > 1$. The site energies of the electrons and holes $T_{ii}^{c,v}$ are taken to be the mid-band-gap energy E_g.

The Coulomb term H_C in Eq. (16) has the monopole-monopole form

$$H_C = \sum_{ijcvc'v'} (a_i^{c'\dagger} a_i^{c'} - a_i^{v'\dagger} a_i^{v'}) V_{ij} (a_j^{c\dagger} a_j^c - a_j^{v\dagger} a_j^v),$$

where the Coulomb interaction is given by

$$V_{ij} = U_0 \frac{d}{|i - j|d + a_0}. \qquad (18)$$

This is similar to the Ohno coupling used in the Pariser-Parr-Pople Hamiltonian of conjugated molecules.[85–87] U_0 characterizes the interaction strength, a_0 is the spatial cutoff, and d is the lattice constant.

Finally, the dipole interaction with the radiation field has the form

$$H_I = -\mathbf{E}(\mathbf{r}, t) \cdot \hat{\mathbf{P}},$$

where $\mathbf{E}(t, \mathbf{r})$ is given by Eq. (1) and $\hat{\mathbf{P}}$ is the interband polarization operator whose expectation value is

$$\mathbf{P} \equiv \langle \hat{\mathbf{P}} \rangle \equiv \sum_{ijvc} [\mu_{ij}^{vc} p_{ij}^{vc} + \text{c.c.}]. \qquad (19)$$

μ_{ij}^{vc} are interband dipoles and $p_{ij}^{vc} \equiv \langle a_i^v a_j^c \rangle$ are interband coherences. The transition dipole matrix elements μ_{ij}^{vc} are defined in Eqs. (12)–(15). All optical transitions are diagonal in the site indices i and j. For example, Eq. (12) reads

$$\mu_{ij}^{v_1 c_1} = \frac{1}{\sqrt{2}} \mu_0 \sigma^+ \delta_{ij} = \frac{1}{\sqrt{2}} \mu_0 \delta_{ij} (\hat{\mathbf{x}} + i\hat{\mathbf{y}}).$$

To make the numerical calculation more tractable, we neglect the exciton population dynamics and work in the coherent limit, where we consider only two types of density matrices involving single-exciton and two-exciton, respectively.[5] To third order in the radiation field, the equations of motion for the first type of density matrix p_{ij}^{vc} are[21,22,28,50,71,81,82]

$$-i\frac{\partial}{\partial t} p_{ij}^{vc} - \frac{i}{t_{ex}} p_{ij}^{vc}$$

$$= -\sum_n T_{jn}^c p_{in}^{vc} - \sum_m T_{mi}^v p_{mj}^{vc} + V_{ij} p_{ij}^{vc}$$

$$+ \sum_{klv'c'} (V_{kj} - V_{ki} - V_{lj} + V_{li})[(p_{lk}^{v'c'})^* p_{lj}^{v'c'} p_{ik}^{vc'}$$

$$- (p_{lk}^{v'c'})^* p_{lk}^{v'c'} p_{ij}^{vc} - (p_{lk}^{v'c'})^* B_{lkij}^{v'c'vc}]$$

$$+ \mathbf{E}(t) \cdot \left[(\mu_{ij}^{vc})^* - \sum_{klv'c'} (\mu_{il}^{vc'})^* (p_{kl}^{v'c'})^* p_{kj}^{v'c} \right.$$

$$\left. - \sum_{klv'c'} (\mu_{lj}^{v'c})^* (p_{lk}^{v'c'})^* p_{ik}^{vc'} \right], \qquad (20)$$

where t_{ex} describes exciton dephasing time. $B_{lkij}^{v'c'vc} \equiv \langle a_l^{v'} a_k^{c'} a_i^v a_j^c \rangle + p_{lj}^{v'c'} p_{ik}^{vc} - p_{lk}^{v'c'} p_{ij}^{vc}$ is the correlated two-exciton amplitude whose equation of motion is

$$-i\frac{\partial}{\partial t} B_{lkij}^{v'c'vc} - \frac{i}{t_{bi}} B_{lkij}^{v'c'vc}$$

$$= -\sum_m (T_{jm}^c B_{lkim}^{v'c'vc} + T_{mi}^v B_{lkmj}^{v'c'vc} + T_{km}^c B_{lmij}^{v'c'vc}$$

$$+ T_{ml}^v B_{mkij}^{v'c'vc}) + (V_{lk} + V_{lj} + V_{ik} + V_{ij} - V_{li} - V_{kj})$$

$$\times B_{lkij}^{v'c'vc} - (V_{lk} + V_{ij} - V_{li} - V_{kj}) p_{ik}^{vc'}$$

$$\times p_{lj}^{v'c} + (V_{ik} + V_{lj} - V_{li} - V_{kj}) p_{lk}^{v'c'} p_{ij}^{vc}, \qquad (21)$$

where t_{bi} is two-exciton dephasing time.

The total interband polarization is given by Eq. (19), where p_{ij}^{vc} is obtained by solving Eqs. (20) and (21). To single out a given FWM signal, we must keep track of the

spatial Fourier components of the interband polarization contributing to different 2D signals (S_I, S_{II}, and S_{III}). For example, to calculate S_I we need the $\mathbf{k}_I$ component of the interband coherences, $p_{ij}^{vc:[\mathbf{k}_I]}$. The positive-frequency component [first term of Eq. (19)] of the total interband polarization field in this direction is thus given by

$$\mathbf{P}^{[\mathbf{k}_I]}(t_3,t_2,t_1,t) \equiv \sum_{ijvc} \mu_{ij}^{vc} p_{ij}^{vc:[\mathbf{k}_I]}(t_3,t_2,t_1,t). \quad (22)$$

The S_I signal [Eq. (10)] is finally given by

$$\mathbf{S}_I(\Omega_3,t_2,\Omega_1) \equiv \int\int \mathbf{P}^{[\mathbf{k}_I]}(t_3,t_2,t_1,t)e^{i\Omega_1 t_1}e^{i\Omega_3 t_3}dt_1 dt_3$$

$$= \int\int \sum_{ijvc} \mu_{ij}^{vc} p_{ij}^{vc:[\mathbf{k}_I]}(t_3,t_2,t_1,t)e^{i\Omega_1 t_1}e^{i\Omega_3 t_3}dt_1 dt_3, \quad (23)$$

where $p_{ij}^{vc:[\mathbf{k}_I]}$ depend on t_3,t_2,t_1, and t through Eq. (20), as well as pulse envelopes and carrier frequencies [Eq. (1)]. $p_{ij}^{vc:[\mathbf{k}_I]}$ are calculated by expanding Eqs. (20) and (21) in the various wave vector Fourier components.[8] We have only calculated the signals for $t_2=0$, where the third and second pulses coincide. The order by order expansion of Eqs. (20) and (21) to yield the signal is given in Appendix C.

To obtain the S_I signal, we have solved Eqs. (C2)–(C5) for different combinations of (t_3,t_1). The other signals (S_{II} and S_{III}) can be calculated by deriving different sets of coupled nonlinear equations from Eqs. (20) and (21) for the relevant spatial Fourier components.

V. NUMERICAL RESULTS

We have employed the 1D tight-binding model to calculate the 2DCS signal from a 20 nm GaAs/Al$_{0.3}$Ga$_{0.7}$As single quantum well (SQW).[50] For the site energies and carrier coupling energies defined in Eq. (17), we used $T_{i\neq j}^c$ =8 meV, $T_{i\neq j}^{v=1,2}$=4.75 meV (HH band), and $T_{i\neq j}^{v=3,4}$ =2.52 meV (LH band) to account for the in-plane dispersion of the valence-band structure in the quantum well.[28,88] The site energies $T_{i=j}^c$ and $T_{i=j}^{v=1,2}$ are taken to be half of the band gap E_g. We used Gaussian pulse envelopes $\mathcal{E}_j^\pm(t-t_j)$ =$\exp[-(t-t_j)^2/\delta_j^2]$, where δ_j=0.3 ps, corresponding to a spectral bandwidth of around 5 meV (full width at half maximum). This narrow bandwidth excludes the continuum states and allows us to control the relative strength of the LH and HH exciton transitions by tuning the carrier frequency, since it is comparable to the LH and HH splittings (3.8 meV) of the SQW sample. The pulse power spectra and the linear absorption are shown in Fig. 7. Calculational details are presented in Appendix D.

Because the oscillator strengths of LH excitons are approximately one-third of those of HH excitons, we have tuned the carrier frequencies of the three optical pulses ω_1 =ω_2=$\omega_3 \equiv \omega_c$ to ω_c=3 meV (Fig. 7, dotted), which enhances the LH exciton transitions. The frequency scale in Fig. 7 and all remaining figures are relative to the HH exciton resonance, which is 35 meV below the band gap.
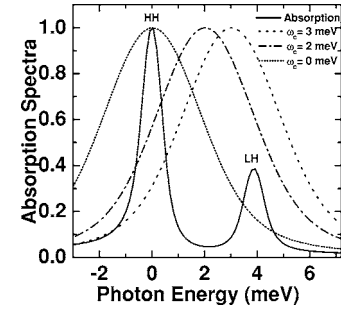

FIG. 7. (Solid): Simulated linear absorption of the single quantum well (see text for parameters). Also shown are optical pulse power spectra $|\mathbf{E}_{opt}(\omega)|^2$ [Eq. (D3)] for ω_c=3 meV (dotted), ω_c =2 meV (dash dot), and ω_c=0 meV (short dot).

To calculate the 2D spectra, we first computed $\mathbf{P}^{[\mathbf{k}_I]}$ for fixed t_1 from t_3=0 to 32 ps with 660 time grid points by solving Eqs. (C2)–(C5). These calculations were then repeated by varying t_1 from 2 to 18 ps on a 330-point grid. The computation time scales as the number of equations, i.e., $64N^4$, where N is the number of sites. We chose t_{ex}=2 ps and t_{bi}=1 ps rather than t_{ex}=4 ps and t_{bi}=2 ps for the dephasing times of excitons and two-excitons, as in Ref. 50. The numerical simulations converge better for faster dephasing rates but at the expense of the spectral resolution. The current values of dephasing times (2 ps/1 ps for excitons and two-excitons) do not show two-exciton peaks but merely reveal shoulders. In all calculations, we employed periodic boundary conditions for N=10. Adding more sites did not have significant effect on our calculations. In Fig. 8, we show $|\mathbf{S}_I(\Omega_3,t_2,t_1,)|$ for t_1=2 ps for different basis size N =10, 12, 14, and 16. The main features of the spectra have converged at N=10. Higher energy (>8 meV) peaks represent continuum states. These do not converge at N=10. However, for the narrow pulse bandwidth used (Fig. 7), the contribution of these continuum states is very small. Testing the convergence is expensive. A single 1DFWM calculation with 16 (18) sites for current parameters takes more than 20 (32) h on a single processor (64 bit Opteron). We thus tested the convergence of 1DFWM signal before launching the
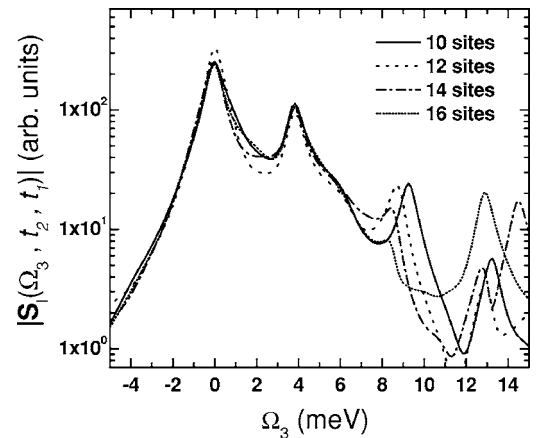

FIG. 8. Convergence of the modulus $|\mathbf{S}_I(\Omega_3,t_2,t_1)|$ with basis size. The 0–6 meV region has converged for N=10. The higher energy continuum has not converged.
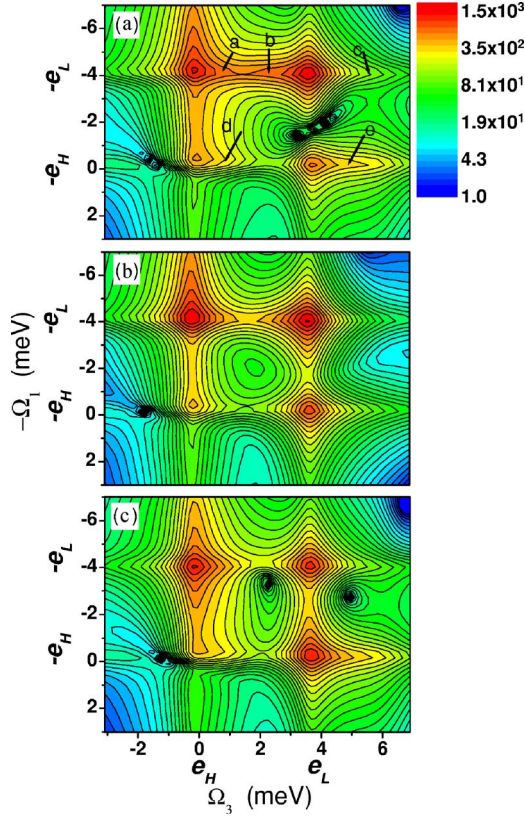
FIG. 9. (Color online) (a) The modulus $|\mathbf{S}_I(\Omega_3,t_2,-\Omega_1)|$ for colinearly polarized pulses (*XX*) (ω_c=3 meV). (b) Same as (a) but excluding two-exciton contributions. (c) Same as (a) but with $\sigma^+\sigma^+$ excitation.

FIG. 10. (Color online) (a) The modulus $|\mathbf{S}_I(\Omega_3,t_2,-\Omega_1)|$ calculated with colinearly polarized pulse excitations (ω_c=2 meV). (b) Same as (a) but excluding the two-exciton contributions.

2DCS calculations. Fast Fourier transform of the 660×330 grid of $\mathbf{P}^{[\mathbf{k}_I]}(t_3,t_2,t_1,t)$ with respect to t_1 and t_3 gave $\mathbf{S}_I(\Omega_3,t_2,-\Omega_1)$. The typical computational time for one 2D plot for N=10 is around 1000 h on a single processor (64 bit Opteron).

The calculated $|\mathbf{S}_I(\Omega_3,t_2,-\Omega_1)|$ signal with two colinearly polarized pulses (hereafter referred to as *XX* excitation) is shown in Fig. 9(a) (log scale).

The two diagonal peaks $(e_H,-e_H)$ and $(e_L,-e_L)$ describe, respectively, the HH and LH excitons. Since the pulse is tuned closer to the LH exciton resonance, the peak $(e_L,-e_L)$ is stronger than $(e_H,-e_H)$. The two major cross peaks $(e_H,-e_L)$ [pathways (ic) and (iic)] and $(e_L,-e_H)$ [pathways (id) and (iid)] describe the coherences which lead to quantum beating among LH and HH excitons. These pathways may be separated using $\mathbf{S}_I(\Omega_3,\Omega_2,t_1)$ as shown in Fig. 13 or the $\mathbf{S}_{II}$ technique (Appendix A).

To show the two-exciton signatures in Fig. 9(a), we have calculated the 2D spectra without the two-exciton contributions [Fig. 9(b)] obtained by neglecting the term $B_{lkij}^{v'c'vc}$ in Eq. (C2). Comparing Figs. 9(a) and 9(b), we can clearly see a feature (e) in Fig. 9(a) for mixed unbound two-excitons. This corresponds to pathways (iiia′) and (iiid). Further separation of these two pathways can be accomplished using other techniques as described in Fig. 13 or in Appendix A. All the two-exciton peaks appear as shoulders adjacent to
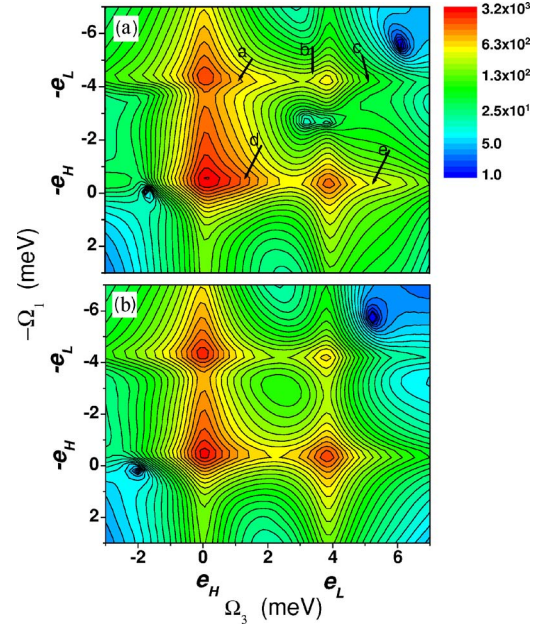
major single-exciton peaks, or as a broadening of the single-exciton peaks.

The two-exciton feature (b) in Fig. 9(a) can be attributed to the bound LH two-excitons discussed in Fig. 6(a) and is visible since the optical pulse enhances the LH excitons as compared to HH excitons. Other two-exciton contributions are also seen in Fig. 9(a). For example, a weak shoulder (c) and two shoulders (a) and (d) are seen in Fig. 9(a), but not in Fig. 9(b). As expected, the two contributions (a) and (d) become stronger as the pulses are further tuned to the red [see Fig. 10(a)]. Finally, by comparing the 2D plots (not shown) with and without the term including the factor $\mathbf{E}(t)$ in Eq. (C2), we found that the contribution from Pauli blocking[89] is negligible.

To study the dependence of $\mathbf{S}_I$ on the pulse polarization configuration, we have calculated the spectra with $\sigma^+\sigma^+$ excitation. These spectra shown in Fig. 9(c) are similar to Fig. 9(a). However, the signature of bound LH two-exciton, the shoulder (b) in Fig. 9(a), is now absent. This is because, according to the selection rules shown in Fig. 3, $\sigma^+\sigma^+$ excitation cannot generate either bound HH two-excitons or bound LH two-excitons.

Figure 10(a) shows the 2D spectrum when the carrier frequency is tuned to ω_c=2 meV (Fig. 7, dashed dot). The 2D spectra calculated without two-exciton contributions is shown in Fig. 10(b).

The effect of tuning is demonstrated by comparing Fig. 10(a) (ω_c=2 meV) and Fig. 9(a) (ω_c=3 meV). The strongest exciton peak $(e_L,-e_L)$ in Fig. 9(a) becomes the weakest in Fig. 10(a), while the weakest exciton peak $(e_H,-e_H)$ in Fig. 9(a) becomes the strongest in Fig. 10(a). Furthermore, because the LH excitons are no longer enhanced for ω_c=2 meV, the signature of the LH bound two-excitons, the shoulder (b) in Fig. 9(a), is absent in Fig. 10(a). The two-
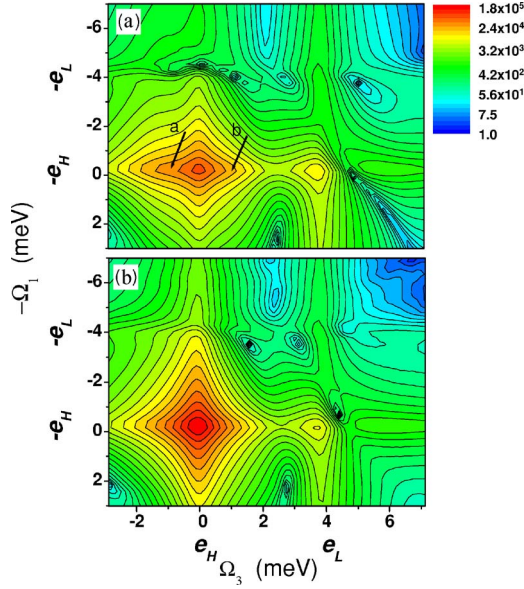
FIG. 11. (Color online) (a) The modulus $|\mathbf{S}_I(\Omega_3, t_2, -\Omega_1)|$ calculated with cross-linearly (XY) polarized pulse excitations $(\omega_c = 0$ meV). (b) Same as (a) but excluding the two-exciton contributions.

FIG. 12. (Color online) $\mathrm{Re}(\mathbf{S}_I(\Omega_3, t_2, -\Omega_1))$ calculated with XX excitation for (a) $\omega_c = 0$ meV, (b) $\omega_c = 2$ meV, and (c) $\omega_c = 3$ meV.

exciton features (c) and (e) in Fig. 9(a) become weaker in Fig. 10(a). However, the two-exciton contributions (a) and (d) in Fig. 10(a) become stronger.

By further redshifting the carrier frequency to $\omega_c = 0$ meV (short dot in Fig. 7) and using cross-linear (XY) polarization (first pulse is polarized in the X direction and the second in the Y direction), we obtain the 2D spectra in Fig. 11(a). For this excitation condition, the pulses are resonant with the HH excitons, and LH excitons are barely excited. Due to the narrow spectral pulse bandwidth, the LH and HH excitons are weakly coupled and the $(e_L, -e_H)$ and $(e_H, -e_L)$ peaks are very weak. For two-exciton contributions, we can clearly see a shoulder (a) for bound HH two-excitons and a broadening (b) for unbound HH two-excitons, as compared to Fig. 11(b) where two-exciton contributions are excluded. The two-exciton contributions are more evident for XY excitation due to strong cancellations of the excitonic signal components.[82] Experimental measurements of the XY configuration also show the elongation along the Ω_3 axis,[90] consistent with the calculated spectrum.

We have further calculated the phase-sensitive 2D spectra rather than their modulus. $\mathrm{Re}(\mathbf{S}_I(\Omega_3, t_2, -\Omega_1))$, calculated with $\omega_c = 0$ meV (XX), is shown in Fig. 12(a). The peak $(e_H, -e_H)$ resembles that experimentally observed (peak RA of Fig. 2 in Ref. 51). The 2D spectra in Fig. 12 is plotted in the same way as in Ref. 51.

The sum-over-states expression for $\mathbf{S}_I$ [Eq. (11)] may be used to interpret the phase-sensitive spectra in Fig. 12(a). For the two-pulse scheme $(t_2 = 0)$ and colinear excitation, we define the real parameter $C \equiv e^{-\Gamma_{gg} t_2} (\mathbf{e}_1 \cdot \boldsymbol{\mu}_{ge'}) (\mathbf{e}_2 \cdot \boldsymbol{\mu}_{e'g})$ $\times (\mathbf{e}_4 \cdot \boldsymbol{\mu}_{ge}) (\mathbf{e}_3 \cdot \boldsymbol{\mu}_{eg}) \mathcal{E}_3^+ \mathcal{E}_2^+ \mathcal{E}_1^-$, where we assume that the $\mathcal{E}_3^+ \mathcal{E}_2^+ \mathcal{E}_1^-$ is real. Moreover, for colinear excitation, the two-exciton contributions from the third term in Eq. (11) are small and will be neglected. We further assume the carrier frequencies $\omega_1 = \omega_2 = \omega_3 \equiv \omega_c$. Equation (11) then gives
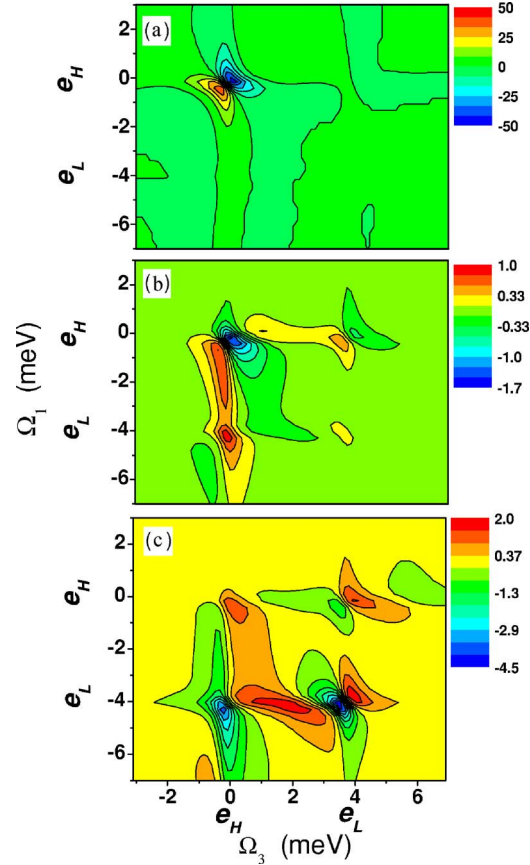
$$S_I^{(3)}(\Omega_3, t_2, -\Omega_1) = \sum_{e,e'} \frac{C}{[\Omega_3 - \widetilde{\omega}_{eg} + i\Gamma_{eg}][\Omega_1 + \widetilde{\omega}_{e'g} + i\Gamma_{e'g}]}$$
$$+ \sum_{e,e'} \frac{C}{[\Omega_3 - \widetilde{\omega}_{eg} + i\Gamma_{eg}][\Omega_1 + \widetilde{\omega}_{e'g} + i\Gamma_{e'g}]}$$
$$= \sum_{e,e'} \frac{2C}{[\Omega_3 - \widetilde{\omega}_{eg} + i\Gamma_{eg}][\Omega_1 + \widetilde{\omega}_{e'g} + i\Gamma_{e'g}]},$$
(24)

where $\widetilde{\omega}_{eg} \equiv \omega_{eg} - \omega_c$ and $\widetilde{\omega}_{e'g} \equiv \omega_{e'g} - \omega_c$. We rewrite Eq. (24) as

$$S_I^{(3)}(\Omega_3, t_2, -\Omega_1)$$
$$= \sum_{e,e'} \frac{2C[(\Omega_3 - \widetilde{\omega}_{eg}) - i\Gamma_{eg}][(\Omega_1 + \widetilde{\omega}_{e'g}) - i\Gamma_{e'g}]}{[(\Omega_3 - \widetilde{\omega}_{eg})^2 + \Gamma_{eg}^2][(\Omega_1 + \widetilde{\omega}_{e'g})^2 + \Gamma_{e'g}^2]},$$
(25)

and thus

$$\text{Re}[S_I^{(3)}(\Omega_3, t_2, -\Omega_1)]$$

$$= \sum_{e,e'} \frac{2C(\Omega_3 - \tilde{\omega}_{eg})(\Omega_1 + \tilde{\omega}_{e'g}) - 2C\Gamma_{eg}\Gamma_{e'g}}{[(\Omega_3 - \tilde{\omega}_{eg})^2 + \Gamma_{eg}^2][(\Omega_1 + \tilde{\omega}_{e'g})^2 + \Gamma_{e'g}^2]}.$$

$$(26)$$

For the excitation of only HH exciton as in Fig. 12(a), Eq. (26) is simplified as

$$\text{Re}[S_I^{(3)}(\Omega_3, t_2, -\Omega_1)]$$

$$= \frac{2C[(\Omega_3 - \tilde{\omega}_{HH})(\Omega_1 + \tilde{\omega}_{HH}) - \Gamma_{HH}^2]}{[(\Omega_3 - \tilde{\omega}_{HH})^2 + \Gamma_{HH}^2][(\Omega_1 + \tilde{\omega}_{HH})^2 + \Gamma_{HH}^2]}, \quad (27)$$

where $\tilde{\omega}_{HH}$ is the HH exciton transition frequency relative to the carrier frequency and Γ_{HH} is the exciton dephasing rate.

Equation (27) accounts for the main features of Fig. 12(a). The denominator gives the resonance peak at $\Omega_3 = \tilde{\omega}_{HH}$ and $\Omega_1 = -\tilde{\omega}_{HH}$, while the numerator gives the positive and/or negative feature. When neglecting Γ_{HH}^2, we see that if Ω_3 goes from below to above $\tilde{\omega}_{HH}$, the signal will change sign for fixed Ω_1. Similarly, when Ω_1 is scanned across $-\tilde{\omega}_{HH}$, the signal will also change sign for fixed Ω_3. In the region where the signal changes signs, steep gradient occurs in the form of the dense contour lines in the center of the blue and/or red peak shown in Fig. 12(a). The zero line along which the steepest local gradient occurs must pass through the peak center $(\tilde{\omega}_{HH}, -\tilde{\omega}_{HH})$, as at this point, Eq. (27) vanishes when Γ_{HH}^2 is neglected. However, for finite Γ_{HH}^2, Eq. (27) is finite at $(\tilde{\omega}_{HH}, -\tilde{\omega}_{HH})$, and thus the zero contour line with steepest local gradient, or the line passing through the center of the negative (positive) [blue (red)] peak, will not pass through the point $(\tilde{\omega}_{HH}, -\tilde{\omega}_{HH})$, which is on the diagonal line. Thus, due to the finite dephasing, the peak center will be off the diagonal line. Because Γ_{HH}^2 is dominated by Coulomb interactions beyond first order (carrier-carrier scattering), the asymmetry of the peaks and their offset from the diagonal lines may provide insights on these many-body correlations. The above analysis applies only to the excitation of a single level, e.g., HH excitons. The picture will become more complicated if a multilevel system is excited.

The calculated 2D spectra (real part) with carrier frequency $\omega_c = 2$ meV (XX) shown in Fig. 12(b) share some similarities with recent experiments,[51] especially for the main peak $(e_H, -e_H)$. However, it is difficult to produce 2D spectra with all four peaks observed in the experiment. In our

calculations, we use a different SQW as compared to the experiment. A two-pulse scheme is employed in our simulations, while the experiment was done with three pulses. In addition, the 2D spectra are very sensitive to the carrier frequency of the narrow-spectra optical pulses and to the parameters such as site energies and hopping and dephasing rates for the HH and LH excitons. For example, by tuning the pulse frequency to the blue [$\omega_c = 3$ meV (XX)], the real signal [Fig. 12(c)] changes considerably compared to Fig. 12(b). The experimental data also show strong dependences on tuning of the excitation pulses as well as their strength.[51,52] Finally, incorporating the population dynamics and continuum states will be required to fully reproduce the experimental spectra.

VI. CONCLUSIONS

As in NMR, optical 2D techniques supplement traditional 1D techniques by revealing microscopic couplings, coherences, and many-body correlations. Using the Liouville pathway analysis, we have predicted the exciton and two-exciton contributions to 2DCS in a single quantum well with LH and HH exciton couplings. Numerical simulations reproduce the major diagonal peaks and cross peaks in a 2D spectra. We also obtained several features from two-exciton contributions. Different 2D techniques provide complementary information.

Some features predicted by the sum-over-states expressions, for example, the bound mixed two-excitons, are not seen in our simulations. This may be due to the small binding energies of these bound two-excitons and to the excitation conditions used. Future extension of the current two-pulse scheme to three pulses[91] and exploring the t_2-dependent 2D spectra will be of interest.

APPENDIX A: THE S_{II} AND S_{III} TECHNIQUES

The response function for the $\mathbf{k}_{II} = \mathbf{k}_1 - \mathbf{k}_2 + \mathbf{k}_3$ signal is given by

$$R_{II}^{(3)}(t_3, t_2, t_1) = i^3 \sum_{e,e'} (\mathbf{e}_4 \cdot \boldsymbol{\mu}_{ge'})(\mathbf{e}_3 \cdot \boldsymbol{\mu}_{e'g})(\mathbf{e}_2 \cdot \boldsymbol{\mu}_{ge})(\mathbf{e}_1 \cdot \boldsymbol{\mu}_{eg})e^{-(i\omega_{e'g} + \Gamma_{e'g})t_3 - \Gamma_{gg}t_2 - (i\omega_{eg} + \Gamma_{eg})t_1} + i^3 \sum_{e,e'} (\mathbf{e}_2 \cdot \boldsymbol{\mu}_{ge'})(\mathbf{e}_3 \cdot \boldsymbol{\mu}_{e'g})(\mathbf{e}_4 \cdot \boldsymbol{\mu}_{ge})$$

$$\times (\mathbf{e}_1 \cdot \boldsymbol{\mu}_{eg})e^{-(i\omega_{eg} + \Gamma_{eg})t_3 - (i\omega_{ee'} + \Gamma_{ee'})t_2 - (i\omega_{eg} + \Gamma_{eg})t_1} - i^3 \sum_{e,e'} \sum_f (\mathbf{e}_2 \cdot \boldsymbol{\mu}_{ge'})(\mathbf{e}_4 \cdot \boldsymbol{\mu}_{e'f})(\mathbf{e}_3 \cdot \boldsymbol{\mu}_{fe})$$

$$\times (\mathbf{e}_1 \cdot \boldsymbol{\mu}_{eg})e^{-(i\omega_{fe'} + \Gamma_{fe'})t_3 - (i\omega_{ee'} + \Gamma_{ee'})t_2 - (i\omega_{eg} + \Gamma_{eg})t_1}, \quad (A1)$$

where the three terms are represented by the Feynman diagrams (iv), (v), and (vi) of Fig. 1, respectively. Substituting Eq. (A1) into Eq. (6) gives the time-domain signal $S_{II}(t_3, t_2, t_1)$. The 2D correlation plot is then obtained by Fourier transforming $S_{II}(t_3, t_2, t_1)$ with respect to t_1 and t_3, holding t_2 fixed, i.e.,

$$S_{\text{II}}^{(3)}(\Omega_3, t_2, \Omega_1) \equiv \int\int dt_3 dt_1 S_{\text{II}}(t_3, t_2, t_1) e^{i\Omega_3 t_3} e^{i\Omega_1 t_1}. \tag{A2}$$

We get

$$\begin{aligned}
S_{\text{II}}^{(3)}(\Omega_3, t_2, \Omega_1) = &\sum_{e,e'} \frac{e^{-\Gamma_{gg}t_2}(\mathbf{e}_4 \cdot \boldsymbol{\mu}_{ge'})(\mathbf{e}_3 \cdot \boldsymbol{\mu}_{e'g})(\mathbf{e}_2 \cdot \boldsymbol{\mu}_{ge})(\mathbf{e}_1 \cdot \boldsymbol{\mu}_{eg})\mathcal{E}_3^+ \mathcal{E}_2^- \mathcal{E}_1^+}{[\Omega_3 - \omega_{e'g} + \omega_3 - \omega_2 + \omega_1 + i\Gamma_{e'g}][\Omega_1 - \omega_{eg} + \omega_1 + i\Gamma_{eg}]} \\
&+ \sum_{e,e'} \frac{e^{-(i\omega_{ee'} + \Gamma_{ee'})t_2}(\mathbf{e}_2 \cdot \boldsymbol{\mu}_{ge'})(\mathbf{e}_3 \cdot \boldsymbol{\mu}_{e'g})(\mathbf{e}_4 \cdot \boldsymbol{\mu}_{ge})(\mathbf{e}_1 \cdot \boldsymbol{\mu}_{eg})\mathcal{E}_3^+ \mathcal{E}_2^- \mathcal{E}_1^+}{[\Omega_3 - \omega_{eg} + \omega_3 - \omega_2 + \omega_1 + i\Gamma_{eg}][\Omega_1 - \omega_{eg} + \omega_1 + i\Gamma_{eg}]} \\
&- \sum_{e,e'}\sum_{f} \frac{e^{-(i\omega_{ee'} + \Gamma_{ee'})t_2}(\mathbf{e}_2 \cdot \boldsymbol{\mu}_{ge'})(\mathbf{e}_4 \cdot \boldsymbol{\mu}_{e'f})(\mathbf{e}_3 \cdot \boldsymbol{\mu}_{fe})(\mathbf{e}_1 \cdot \boldsymbol{\mu}_{eg})\mathcal{E}_3^+ \mathcal{E}_2^- \mathcal{E}_1^+}{[\Omega_3 - \omega_{fe'} + \omega_3 - \omega_2 + \omega_1 + i\Gamma_{fe'}][\Omega_1 - \omega_{eg} + \omega_1 + i\Gamma_{eg}]}.
\end{aligned} \tag{A3}$$

The response function for the $\mathbf{k}_{\text{III}} = \mathbf{k}_1 + \mathbf{k}_2 - \mathbf{k}_3$ signal is given by

$$\begin{aligned}
R_{\text{III}}^{(3)}(t_3, t_2, t_1) = &i^3 \sum_{e,e'}\sum_{f}(\mathbf{e}_4 \cdot \boldsymbol{\mu}_{ge'})(\mathbf{e}_3 \cdot \boldsymbol{\mu}_{e'f})(\mathbf{e}_2 \cdot \boldsymbol{\mu}_{fe})(\mathbf{e}_1 \cdot \boldsymbol{\mu}_{eg})e^{-(i\omega_{e'g} + \Gamma_{e'g})t_3 - (i\omega_{fg} + \Gamma_{fg})t_2 - (i\omega_{eg} + \Gamma_{eg})t_1} - i^3 \sum_{e,e'}\sum_{f}(\mathbf{e}_3 \cdot \boldsymbol{\mu}_{ge'})(\mathbf{e}_4 \cdot \boldsymbol{\mu}_{e'f}) \\
&\times (\mathbf{e}_2 \cdot \boldsymbol{\mu}_{fe})(\mathbf{e}_1 \cdot \boldsymbol{\mu}_{eg})e^{-(i\omega_{fe'} + \Gamma_{fe'})t_3 - (i\omega_{fg} + \Gamma_{fg})t_2 - (i\omega_{eg} + \Gamma_{eg})t_1},
\end{aligned} \tag{A4}$$

where the two terms correspond to the Feynman diagrams (vii) and (viii) in Fig. 1. Substituting Eq. (A4) into Eq. (7) gives the time-domain signal $S_{\text{III}}(t_3, t_2, t_1)$. The 2D correlation spectra are obtained by Fourier transform $S_{\text{III}}(t_3, t_2, t_1)$ with respect to t_2 and t_3, holding t_1 fixed,

$$S_{\text{III}}^{(3)}(\Omega_3, \Omega_2, t_1) \equiv \int\int dt_3 dt_1 S_{\text{III}}(t_3, t_2, t_1) e^{i\Omega_3 t_3} e^{i\Omega_2 t_2}.$$

This gives

$$\begin{aligned}
S_{\text{III}}^{(3)}(\Omega_3, \Omega_2, t_1) = &\sum_{e,e'}\sum_{f} \frac{e^{-(i\omega_{eg} + \Gamma_{eg})t_1}(\mathbf{e}_4 \cdot \boldsymbol{\mu}_{ge'})(\mathbf{e}_3 \cdot \boldsymbol{\mu}_{e'f})(\mathbf{e}_2 \cdot \boldsymbol{\mu}_{fe})(\mathbf{e}_1 \cdot \boldsymbol{\mu}_{eg})\mathcal{E}_3^- \mathcal{E}_2^+ \mathcal{E}_1^+}{[\Omega_3 - \omega_{e'g} - \omega_3 + \omega_2 + \omega_1 + i\Gamma_{e'g}][\Omega_2 - \omega_{fg} + \omega_1 + \omega_2 + i\Gamma_{fg}]} \\
&- \sum_{e,e'}\sum_{f} \frac{e^{-(i\omega_{eg} + \Gamma_{eg})t_1}(\mathbf{e}_3 \cdot \boldsymbol{\mu}_{ge'})(\mathbf{e}_4 \cdot \boldsymbol{\mu}_{e'f})(\mathbf{e}_2 \cdot \boldsymbol{\mu}_{fe})(\mathbf{e}_1 \cdot \boldsymbol{\mu}_{eg})\mathcal{E}_3^- \mathcal{E}_2^+ \mathcal{E}_1^+}{[\Omega_3 - \omega_{fe'} - \omega_3 + \omega_2 + \omega_1 + i\Gamma_{fe'}][\Omega_2 - \omega_{fg} + \omega_1 + \omega_2 + i\Gamma_{fg}]}.
\end{aligned} \tag{A5}$$

S_{II} and S_{III} techniques provide complementary information to the S_{I} technique. S_{III} technique is particularly sensitive to exciton-exciton coupling. The 2D spectra of techniques S_{II} and S_{III} can be similarly analyzed as in the S_{I} technique.

APPENDIX B: ALTERNATIVE 2D PROJECTION OF THE S_I SIGNAL

The bound mixed two-excitons from different pathways (e.g., solid trapezoid and square) not resolved in Fig. 6(a) may be separated by displaying the $\mathbf{S}_{\text{I}}$ 2D spectra with different variables such as $(\Omega_3, \Omega_2, t_1)$ rather than $(\Omega_3, t_2, -\Omega_1)$, or by employing other 2D techniques (Appendix A). In Fig. 13, we display $\mathbf{S}_{\text{I}}(\Omega_3, \Omega_2, t_1)$. Panels (a) and (b) correspond to the Feynman diagrams in Fig. 4, and panel (c) corresponds to the Feynman diagrams in Fig. 5. Panel (d) shows the total spectrum from the diagrams of Figs. 4 and 5, where the single-exciton contributions along Ω_3 [from Figs. 13(a) and 13(b)] are represented by two open vertical ovals.
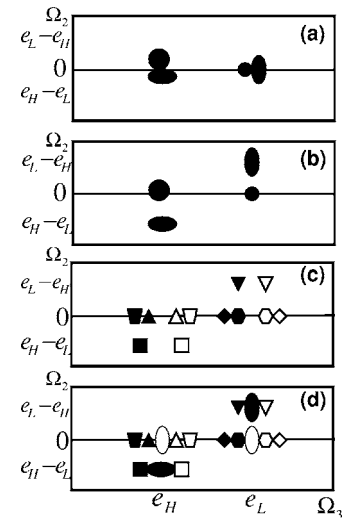

FIG. 13. The $\mathbf{S}_{\text{I}}(\Omega_3, \Omega_2, t_1)$ signal. (a) Diagrams (ia), (ib), (ic), and (id). (b) Diagrams (iia), (iib), and (iic). (c) Diagrams (iiia)–(iiid). (d) Total spectrum.

$\mathbf{S}_I(\Omega_3, \Omega_2, t_1)$ can resolve peaks indistinguishable in $\mathbf{S}_I(\Omega_3, t_2, -\Omega_1)$. For example, (ic) and (iic) (both denoted by a horizontal oval) overlap at $(e_H, -e_L)$ in Fig. 6(a). Similarly, (id) and (iid) (both denoted by a vertical oval) overlap at $(e_L, -e_H)$. The two-exciton contributions denoted by a solid trapezoid and a solid square in Fig. 6(a) also overlap. The same holds for the two-exciton contributions denoted by a solid hexagon and a solid inverted triangle in Fig. 6(a). However, all of these overlapping couplings can be easily resolved by $\mathbf{S}_I(\Omega_3, \Omega_2, t_1)$. In Fig. 13(a), pathways (ia) and (ic) both contribute to the peak $(\Omega_3, \Omega_2) = (e_H, 0)$ (displaced in the figure for clarity). However, pathway (iic) now gives a peak at $(e_H, e_H - e_L)$ [Fig. 13(b)] and is thus well separated from (ic), in contrast to $\mathbf{S}_I(\Omega_3, t_2, -\Omega_1)$ (Fig. 4) where these two pathways overlapped. Similarly, pathway (iid) appears at $(e_L, e_L - e_H)$ [Fig. 13(b)] and is thus separated from (id), which appears at $(e_L, 0)$ in Fig. 13(a). Thus, $\mathbf{S}_I(\Omega_3, \Omega_2, t_1)$

(Fig. 13) provides a complementary information by separating different pathways which overlap in $\mathbf{S}_I(\Omega_3, t_2, -\Omega_1)$ [Fig. 6(a)]. All two-exciton contributions to Fig. 5 are plotted in Fig. 13(c). Figure 13(c) also provides complementary information to $\mathbf{S}_I(\Omega_3, t_2, -\Omega_1)$ [Fig. 6(a)]. For example, the mixed two-excitons from two pathways (solid square and a trapezoid) overlap in Fig. 6(a) but are well separated in Fig. 13(c). The same holds for the solid hexagon and solid inverted triangle.

APPENDIX C: SELECTING SPATIAL FOURIER COMPONENTS OF INTERBAND POLARIZATIONS

In this appendix, we present the equations of motion used for calculating FWM signals for a two-pulse scheme ($t_2 = 0$). According to Eq. (20), the $\mathbf{k}_I$ spatial component of interband density matrix, $p_{ij}^{vc:[\mathbf{k}_I]}$, satisfies

$$-i\frac{\partial}{\partial t}p_{ij}^{vc:[-\mathbf{k}_1+\mathbf{k}_2+\mathbf{k}_2]} - \frac{i}{t_{ex}}p_{ij}^{vc:[-\mathbf{k}_1+\mathbf{k}_2+\mathbf{k}_2]} = -\sum_n T_{jn}^c p_{in}^{vc:[-\mathbf{k}_1+\mathbf{k}_2+\mathbf{k}_2]} - \sum_m T_{mi}^v p_{mj}^{vc:[-\mathbf{k}_1+\mathbf{k}_2+\mathbf{k}_2]} + V_{ij}p_{ij}^{vc:[-\mathbf{k}_1+\mathbf{k}_2+\mathbf{k}_2]}$$

$$+ \sum_{klv'c'}(V_{kj} - V_{ki} - V_{lj} + V_{li})\{[(p_{lk}^{v'c'})^* p_{lj}^{v'c} p_{ik}^{vc'}]^{[-\mathbf{k}_1+\mathbf{k}_2+\mathbf{k}_2]}$$

$$- [(p_{lk}^{v'c'})^* p_{lk}^{v'c'} p_{ij}^{vc}]^{:[-\mathbf{k}_1+\mathbf{k}_2+\mathbf{k}_2]} - [(p_{lk}^{v'c'})^* B_{lkij}^{v'c'vc}]^{:[-\mathbf{k}_1+\mathbf{k}_2+\mathbf{k}_2]}\}$$

$$- \sum_{klv'c'}\{(\mu_{il}^{vc'})^* \cdot [\mathbf{E}(t)(p_{kl}^{v'c'})^* p_{kj}^{v'c}]^{[-\mathbf{k}_1+\mathbf{k}_2+\mathbf{k}_2]} + (\mu_{lj}^{v'c})^* \cdot [\mathbf{E}(t)(p_{lk}^{v'c'})^* p_{ik}^{vc'}]^{[-\mathbf{k}_1+\mathbf{k}_2+\mathbf{k}_2]}\}.$$

(C1)

To first order in the optical field, the single-exciton density matrix p contains either $\mathbf{k}_1$ or $\mathbf{k}_2$. Invoking the rotating wave approximation (RWA) and by a perturbative expansion[8,82] to third order in the optical field, Eq. (C1) becomes

$$-i\frac{\partial}{\partial t}p_{ij}^{vc:[-\mathbf{k}_1+\mathbf{k}_2+\mathbf{k}_2]} - \frac{i}{t_{ex}}p_{ij}^{vc:[-\mathbf{k}_1+\mathbf{k}_2+\mathbf{k}_2]} = -\sum_n T_{jn}^c p_{in}^{vc:[-\mathbf{k}_1+\mathbf{k}_2+\mathbf{k}_2]} - \sum_m T_{mi}^v p_{mj}^{vc:[-\mathbf{k}_1+\mathbf{k}_2+\mathbf{k}_2]} + V_{ij}p_{ij}^{vc:[-\mathbf{k}_1+\mathbf{k}_2+\mathbf{k}_2]}$$

$$+ \sum_{klv'c'}(V_{kj} - V_{ki} - V_{lj} + V_{li})\{[(p_{lk}^{v'c':\mathbf{k}_1})^* p_{lj}^{v'c:\mathbf{k}_2} p_{ik}^{vc':\mathbf{k}_2}] - [(p_{lk}^{v'c':\mathbf{k}_1})^* p_{lk}^{v'c':\mathbf{k}_2} p_{ij}^{vc:\mathbf{k}_2}]$$

$$- [(p_{lk}^{v'c':\mathbf{k}_1})^* B_{lkij}^{v'c'vc:[\mathbf{k}_2+\mathbf{k}_2]}]\} + \mathbf{E}_2(t) \cdot \sum_{klv'c'}\{(\mu_{il}^{vc'})^*(p_{kl}^{v'c':\mathbf{k}_1})^* p_{kj}^{v'c:\mathbf{k}_2}$$

$$+ (\mu_{lj}^{v'c})^*(p_{lk}^{v'c':\mathbf{k}_1})^* p_{ik}^{vc':\mathbf{k}_2}\}.$$

(C2)

Apart from the density-matrix element $p_{ij}^{vc:[-\mathbf{k}_1+\mathbf{k}_2+\mathbf{k}_2]}$, Eq. (C2) also contains the matrix elements $p_{ij}^{vc[\mathbf{k}_1]}$, $p_{ij}^{vc[\mathbf{k}_2]}$, and $B_{lkij}^{v'c'vc:[\mathbf{k}_2+\mathbf{k}_2]}$. Thus, to solve for $p_{ij}^{vc:[-\mathbf{k}_1+\mathbf{k}_2+\mathbf{k}_2]}(t_3, t_2, t_1, t)$ at time t, we should calculate $p_{ij}^{vc[\mathbf{k}_1]}(t)$, $p_{ij}^{vc[\mathbf{k}_2]}(t)$, and $B_{lkij}^{v'c'vc:[\mathbf{k}_2+\mathbf{k}_2]}(t)$ simultaneously. Following the similar procedure of deriving Eq. (C2), we obtain the following equations for solving $p_{ij}^{vc[\mathbf{k}_1]}(t)$, $p_{ij}^{vc[\mathbf{k}_2]}(t)$, and $B_{lkij}^{v'c'vc:[\mathbf{k}_2+\mathbf{k}_2]}(t)$:

$$-i\frac{\partial}{\partial t}p_{ij}^{vc[\mathbf{k}_1]} - \frac{i}{t_{ex}}p_{ij}^{vc[\mathbf{k}_1]} = -\sum_n T_{jn}^c p_{in}^{vc[\mathbf{k}_1]} - \sum_m T_{mi}^v p_{mj}^{vc[\mathbf{k}_1]}$$
$$+ V_{ij}p_{ij}^{vc[\mathbf{k}_1]} + \mathbf{E}_1(t) \cdot (\mu_{ij}^{vc})^*, \quad \text{(C3)}$$

$$-i\frac{\partial}{\partial t}p_{ij}^{vc[\mathbf{k}_2]} - \frac{i}{t_{ex}}p_{ij}^{vc[\mathbf{k}_2]} = -\sum_n T_{jn}^c p_{in}^{vc[\mathbf{k}_2]} - \sum_m T_{mi}^v p_{mj}^{vc[\mathbf{k}_2]}$$
$$+ V_{ij}p_{ij}^{vc[\mathbf{k}_2]} + \mathbf{E}_2(t) \cdot (\mu_{ij}^{vc})^*, \quad \text{(C4)}$$

$$- i\frac{\partial}{\partial t}B_{lkij}^{v'c'vc:[\mathbf{k}_2+\mathbf{k}_2]} - \frac{i}{t_{bi}}B_{lkij}^{v'c'vc:[\mathbf{k}_2+\mathbf{k}_2]}$$

$$= -\sum_m (T_{jm}^c B_{lkim}^{v'c'vc:[\mathbf{k}_2+\mathbf{k}_2]} + T_{mi}^v B_{lkmj}^{v'c'vc:[\mathbf{k}_2+\mathbf{k}_2]}$$

$$+ T_{km}^c B_{lmij}^{v'c'vc:[\mathbf{k}_2+\mathbf{k}_2]} + T_{ml}^v B_{mkij}^{v'c'vc:[\mathbf{k}_2+\mathbf{k}_2]})$$

$$+ (V_{lk} + V_{lj} + V_{ik} + V_{ij} - V_{li} - V_{kj})B_{lkij}^{v'c'vc:[\mathbf{k}_2+\mathbf{k}_2]}$$

$$- (V_{lk} + V_{ij} - V_{li} - V_{kj})p_{ik}^{vc'[\mathbf{k}_2]}p_{lj}^{v'c[\mathbf{k}_2]}$$

$$+ (V_{ik} + V_{lj} - V_{li} - V_{kj})p_{lk}^{v'c'[\mathbf{k}_2]}p_{ij}^{vc[\mathbf{k}_2]}. \tag{C5}$$

Solving the set of coupled equations (C2)–(C5) gives $p_{ij}^{vc:[-\mathbf{k}_1+\mathbf{k}_2+\mathbf{k}_2]}(t_3,t_2,t_1,t)$. Substituting $p_{ij}^{vc:[-\mathbf{k}_1+\mathbf{k}_2+\mathbf{k}_2]}(t_3,t_2,t_1,t)$ into Eq. (23) results in the $\mathbf{S}_I$ 2D signal. Equations for the $\mathbf{S}_{II}$ and $\mathbf{S}_{III}$ 2D signals can be derived in a similar way.

APPENDIX D: NUMERICAL CALCULATION OF LINEAR ABSORPTION

From Eqs. (19) and (22), the total polarization along the $\mathbf{k}_I$ direction is written as

$$\mathbf{P}(t) = \mathbf{P}^{[\mathbf{k}_I]}(t_3,t_2,t_1,t) + \text{c.c.}$$

$$= \sum_{ijvc} \mu_{ij}^{vc} p_{ij}^{vc:[\mathbf{k}_I]}(t_3,t_2,t_1,t) + \text{c.c.}$$

$$\equiv \mathbf{p}(t)e^{-i\omega_g t} + \text{c.c.}, \tag{D1}$$

where $\mathbf{p}(t)$ is defined as the slowly varying portion relative to the band gap frequency ω_g. Performing Fourier transform of the polarization relative to ω_g gives

$$\mathbf{P}(\omega) = \int_{-\infty}^{\infty} \mathbf{P}(t)e^{-i(\omega-\omega_g)t}dt$$

$$= \int_{-\infty}^{\infty} [\mathbf{p}(t)e^{-i\omega_g t} + \text{c.c.}]e^{-i(\omega-\omega_g)t}dt$$

$$= \int_{-\infty}^{\infty} [\mathbf{p}(t)e^{-i\omega t} + \mathbf{p}^*(t)e^{-i(\omega-2\omega_g)t}]dt$$

$$\approx \int_{-\infty}^{\infty} \mathbf{p}(t)e^{-i\omega t}dt. \tag{D2}$$

Similarly, performing Fourier transform of the jth optical pulse [Eq. (1)] relative to the band-gap frequency ω_g gives (spatial portion is omitted)

$$\mathbf{E}_{\mathbf{opt}}(\omega) = \int_{-\infty}^{\infty} [\mathcal{E}_j^+ e^{-i\omega_j t} + \text{c.c.}]e^{-i(\omega-\omega_g)t}$$

$$= \int_{-\infty}^{\infty} [\mathcal{E}_j^+ e^{-i(\omega_j-\omega_g)t}e^{-i\omega_g t}e^{-i(\omega-\omega_g)t} + e^{-i(\omega-\omega_g)t}\cdot \text{c.c.}]dt$$

$$\approx \int_{-\infty}^{\infty} \mathcal{E}_j^+ e^{-i(\omega_j-\omega_g)t}e^{-i\omega t}dt, \tag{D3}$$

where $\mathbf{E}_{\text{opt}}(\omega)$ is approximately the Fourier transform of pulse envelope $\mathcal{E}_j^+$ because we consider only resonant excitation where ω_j is close to ω_g. Finally, the linear absorption is calculated as[36,92]

$$\alpha(\omega) = \frac{\omega_j}{n'c\epsilon_0} \text{Im}\left[\frac{\mathbf{P}(\omega)\cdot \mathbf{E}_{\text{opt}}^*(\omega)}{|\mathbf{E}_{\text{opt}}(\omega)|^2}\right], \tag{D4}$$

where n' is the average, frequency-independent refractive index of the quantum well, ϵ_0 is the vacuum permittivity, and c is the speed of light.

[1] X. Li, Y. Wu, D. Steel, D. Gammon, T. H. Stievater, D. S. Katzer, D. Park, C. Piermarocchi, and L. J. Sham, Science **301**, 809 (2003).

[2] S. Mukamel, Annu. Rev. Phys. Chem. **51**, 691 (2000).

[3] H. Haug and S. W. Koch, *Quantum Theory of the Optical and Electronic Properties of Semiconductors*, 3rd ed. (World Scientific, Singapore, 1994).

[4] D. S. Chemla and J. Shah, Nature (London) **411**, 549 (2001).

[5] V. M. Axt and S. Mukamel, Rev. Mod. Phys. **70**, 145 (1998).

[6] M. Wegener, D. S. Chemla, S. Schmitt-Rink, and W. Schäfer, Phys. Rev. A **42**, 5675 (1990).

[7] K. Leo, M. Wegener, J. Shah, D. S. Chemla, E. O. Göbel, T. C. Damen, S. Schmitt-Rink, and W. Schäfer, Phys. Rev. Lett. **65**, 1340 (1990).

[8] M. Lindberg, R. Binder, and S. W. Koch, Phys. Rev. A **45**, 1865 (1992).

[9] M. Bonitz, *Quantum Kinetic Theory*, Teubner-Texte zur Physik Vol. 33 (Teubner-Verlag, Stuttgart, 1998).

[10] U. Hohenester and W. Pötz, Phys. Rev. B **56**, 13177 (1997).

[11] M. F. Pereira and K. Henneberger, Phys. Rev. B **58**, 2064 (1998).

[12] A. L. Ivanov, H. Haug, and L. V. Keldysh, Phys. Rep. **296**, 237 (1998).

[13] N. H. Kwong and R. Binder, Phys. Rev. B **61**, 8341 (2000).

[14] J. Shah, *Ultrafast Spectroscopy of Semiconductors and Semiconductor Nanostructures*, 2nd ed. (Springer, New York, 1999).

[15] H. Haug and A.-P. Jauho, *Quantum Kinetics in Transport and Optics of Semiconductors* (Springer, Berlin, 1996).

[16] F. Rossi and T. Kuhn, Rev. Mod. Phys. **74**, 895 (2002).

[17] V. M. Axt, G. Bartels, and A. Stahl, Phys. Rev. Lett. **76**, 2543 (1996).

[18] G. Bartels, G. C. Cho, T. Dekorsy, H. Kurz, A. Stahl, and K. Köhler, Phys. Rev. B **55**, 16404 (1997).

[19] J. Hader, T. Meier, S. W. Koch, F. Rossi, and N. Linder, Phys. Rev. B **55**, 13799 (1997).

[20] Th. Östreich, K. Schönhammer, and L. J. Sham, Phys. Rev. B **58**, 12920 (1998).

[21] L. Bányai, I. Galbraith, C. Ell, and H. Haug, Phys. Rev. B **36**, 6099 (1987).

[22] C. Sieh, T. Meier, F. Jahnke, A. Knorr, S. W. Koch, P. Brick, M. Hübner, C. Ell, J. Prineas, G. Khitrova, and H. M. Gibbs, Phys.

Rev. Lett. **82**, 3112 (1999); C. Sieh, T. Meier, A. Knorr, F. Jahnke, P. Thomas, and S. W. Koch, Eur. Phys. J. B **11**, 407 (1999).

[23] F. Löser, M. M. Dignam, Yu. A. Kosevich, K. Köhler, and K. Leo, Phys. Rev. Lett. **85**, 4763 (2000).

[24] V. G. Lyssenko, G. Valusis, F. Loser, T. Hasche, K. Leo, M. M. Dignam, and K. Kohler, Phys. Rev. Lett. **79**, 301 (1997).

[25] M. Hawton and M. M. Dignam, Phys. Rev. Lett. **91**, 267402 (2003).

[26] A. L. Smirl, M. J. Stevens, X. Chen, and O. Buccafusca, Phys. Rev. B **60**, 8267 (1999).

[27] M. Phillips and H. Wang, Solid State Commun. **11**, 317 (1999).

[28] T. Meier, S. W. Koch, M. Phillips, and H. Wang, Phys. Rev. B **62**, 12605 (2000).

[29] H. P. Wagner, W. Langbein, and J. M. Hvam, Phys. Rev. B **59**, 4584 (1999).

[30] Y. Tanimura and S. Mukamel, J. Chem. Phys. **99**, 9496 (1993).

[31] V. Chernyak and S. Mukamel, J. Opt. Soc. Am. B **13**, 1302 (1996).

[32] V. Chernyak, W. M. Zhang, and S. Mukamel, J. Chem. Phys. **109**, 9587 (1998).

[33] W. M. Zhang, V. Chernyak, and S. Mukamel, J. Chem. Phys. **110**, 5011 (1999).

[34] S. Mukamel and D. Abramavicius, Chem. Rev. (Washington, D.C.) **104**, 2073–2098 (2004).

[35] W. Zhuang, D. Abramavicius, T. Hayashi, and S. Mukamel, J. Phys. Chem. B **110**, 3362 (2006).

[36] S. Mukamel, *Principles of Nonlinear Optical Spectroscopy* (Oxford University Press, New York, 1995).

[37] R. R. Ernst, G. Bodenhausen, and A. Wokaun *Principles of Nuclear Magnetic Resonance in One and Two Dimensions* (Clarendon, Oxford, 1987).

[38] J. N. Evans, *Biomolecular NMR Spectroscopy* (Oxford University Press, New York, 1995).

[39] S. Mukamel and W. Zhuang, Proc. Natl. Acad. Sci. U.S.A. **102**, 13717 (2005).

[40] W. Zhuang, D. Abramavicius, and S. Mukamel, Proc. Natl. Acad. Sci. U.S.A. **102**, 7443 (2005).

[41] D. Abramavicius and S. Mukamel, J. Chem. Phys. **122**, 134305 (2005).

[42] J. Zheng, K. Kwak, J. Asbury, X. Chen, I. Piletic, and M. D. Fayer, Science **309**, 1338 (2005).

[43] Ch. Kolano, J. Helbing, M. Kozinski, and W. Sander, Nature (London) **444**, 469 (2006).

[44] T. Brixner, J. Stenger, H. M. Vaswani, M. Cho, R. E. Blankenship, and G. R. Fleming, Nature (London) **434**, 625 (2005).

[45] M. C. Asplund, M. T. Zanni, and R. M. Hochstrasser, Proc. Natl. Acad. Sci. U.S.A. **97**, 8219 (2000).

[46] M. Koch, J. Feldmann, G. von Plessen, E. O. Göbel, P. Thomas, and K. Köhler, Phys. Rev. Lett. **69**, 3631 (1996).

[47] V. G. Lyssenko, J. Erland, I. Balslev, K.-H. Pantke, B. S. Razbirin, and J. M. Hvam, Phys. Rev. B **48**, 5720 (1993).

[48] S. T. Cundiff, M. Koch, W. H. Knox, J. Shah, and W. Stolz, Phys. Rev. Lett. **77**, 1107 (1996).

[49] A. Euteneuer, E. Finger, M. Hofmann, W. Stolz, T. Meier, P. Thomas, S. W. Koch, W. W. Rühle, R. Hey, and K. Ploog, Phys. Rev. Lett. **83**, 2073 (1999).

[50] E. Finger, S. Kraft, M. Hofmann, T. Meier, S. W. Koch, W. Stolz, W. W. Rühle, and A. Wieck, Phys. Status Solidi B **234**, 424 (2002).

[51] Xiaoqin Li, Tianhao Zhang, Camelia N. Borca, and Steven T. Cundiff, Phys. Rev. Lett. **96**, 057406 (2006).

[52] C. N. Borca, T. Zhang, X. Li, and S. T. Cundiff, Chem. Phys. Lett. **416**, 311 (2005).

[53] S. Yokojima, T. Meier, V. Chernyak, and S. Mukamel, Phys. Rev. B **59**, 12584 (1999).

[54] W. M. Zhang, T. Meier, V. Chernyak, and S. Mukamel, Phys. Rev. B **60**, 2599 (1999).

[55] C. Scheurer and S. Mukamel, Bull. Chem. Soc. Jpn. **75**, 989 (2002).

[56] N. Demirdöven, M. Khalil, and A. Tokmakoff, Phys. Rev. Lett. **89**, 237401 (2002).

[57] K. Bott, O. Heller, D. Bennhardt, S. T. Cundiff, P. Thomas, E. J. Mayer, G. O. Smith, R. Eccleston, J. Kuhl, and K. Ploog, Phys. Rev. B **48**, 17418 (1993).

[58] A. Piryatinski, S. Tretiak, V. Chernyak, and S. Mukamel, J. Raman Spectrosc. **31**, 125 (2000).

[59] F. C. Spano and S. Mukamel, Phys. Rev. Lett. **66**, 1197 (1991).

[60] F. C. Spano and S. Mukamel, J. Chem. Phys. **95**, 7526 (1991).

[61] J. A. Leegwater and S. Mukamel, Phys. Rev. A **46**, 452 (1992).

[62] S. Mukamel, in *Molecular Nonlinear Optics*, edited by J. Zyss (Academic, New York, 1994), pp. 1–46.

[63] V. M. Axt and A. Stahl, Z. Phys. B: Condens. Matter **93**, 195 (1994).

[64] M. Lindberg, Y. Z. Hu, R. Binder, and S. W. Koch, Phys. Rev. B **50**, 18060 (1994).

[65] K. Bott, E. J. Mayer, G. O. Smith, V. Heuckeroth, M. Hübner, J. Kuhl, T. Meier, A. Schulze, M. Lindberg, S. W. Koch, and P. Thomas, J. Opt. Soc. Am. B **13**, 1026 (1996).

[66] B. F. Feuerbacher, J. Kuhl, and K. Ploog, Phys. Rev. B **43**, 2439 (1991).

[67] E. J. Mayer, G. O. Smith, V. Heuckeroth, J. Kuhl, K. Bott, A. Schulze, T. Meier, S. W. Koch, P. Thomas, R. Hey, and K. Ploog, Phys. Rev. B **51**, 10909 (1995).

[68] E. J. Mayer, G. O. Smith, V. Heuckeroth, J. Kuhl, K. Bott, A. Schulze, T. Meier, D. Bennhardt, S. W. Koch, P. Thomas, R. Hey, and K. Ploog, Phys. Rev. B **50**, 14730 (1994).

[69] S. Bar-Ad and I. Bar-Joseph, Phys. Rev. Lett. **68**, 349 (1992).

[70] D. J. Lovering, R. T. Phillips, G. J. Denton, and G. W. Smith, Phys. Rev. Lett. **68**, 1880 (1992).

[71] K. Bott, J. Hader, S. W. Koch, and P. Thomas, Phys. Rev. B **56**, R12784 (1997).

[72] J.-Y. Bigot, A. Daunois, J. Oberle, and J.-C. Merle, Phys. Rev. Lett. **71**, 1820 (1993).

[73] J.-Y. Bigot, M.-A. Mycek, S. Weiss, R. G. Ulbrich, and D. S. Chemla, Phys. Rev. Lett. **70**, 3307 (1993).

[74] H. Wang, K. B. Ferrio, D. G. Steel, Y. Z. Hu, R. Binder, and S. W. Koch, Phys. Rev. Lett. **71**, 1261 (1993); H. Wang, K. B. Ferrio, D. G. Steel, P. R. Berman, Y. Z. Hu, R. Binder, and S. W. Koch, Phys. Rev. A **49**, R1551 (1994); Y. Z. Hu, R. Binder, S. W. Koch, S. T. Cundiff, H. Wang, and D. G. Steel, Phys. Rev. B **49**, 14382 (1994).

[75] T. Rappen, U. G. Peter, M. Wegener, and W. Schäfer, Phys. Rev. B **49**, 10774 (1994).

[76] T. F. Albrecht, K. Bott, T. Meier, A. Schulze, M. Koch, S. T. Cundiff, J. Feldmann, W. Stolz, P. Thomas, S. W. Koch, and E. O. Göbel, Phys. Rev. B **54**, 4436 (1996).

[77] W. Schäfer, D. S. Kim, J. Shah, T. C. Damen, J. E. Cunningham, K. W. Goossen, L. N. Pfeiffer, and K. Köhler, Phys. Rev. B **53**, 16429 (1996).

[78] P. Kner, S. Bar-Ad, M. V. Marquezini, D. S. Chemla, and W. Schäfer, Phys. Rev. Lett. **78**, 1319 (1997).

[79] F. Jahnke, M. Kira, S. W. Koch, G. Khitrova, E. K. Lindmark, T. R. Nelson, Jr., D. V. Wick, J. D. Berger, O. Lyngnes, H. M. Gibbs, and K. Tai, Phys. Rev. Lett. **77**, 5257 (1996).

[80] S. Mukamel, R. Oszwaldowski, and D. Abramavicius (unpublished).

[81] D. Brinkmann, K. Bott, S. W. Koch, and P. Thomas, Phys. Status Solidi B **206**, 493 (1998).

[82] S. Weiser, T. Meier, J. Möbius, A. Euteneuer, E. J. Mayer, W. Stolz, M. Hofmann, W. W. Rühle, P. Thomas, and S. W. Koch, Phys. Rev. B **61**, 13088 (2000).

[83] T. Meier, P. Thomas, and S. W. Koch, *Coherent Semiconductor Optics: From Basic Concepts to Nanostructure Applications* (Springer, New York, 2006).

[84] M. Z. Maialle and L. J. Sham, Phys. Rev. Lett. **73**, 3310 (1994).

[85] T. Meier and S. Mukamel, Phys. Rev. Lett. **77**, 3471 (1996).

[86] T. Meier, S. Tretiak, V. Chernyak, and S. Mukamel, Phys. Rev. B **55**, 4960 (1997).

[87] H. Fukutome, J. Mol. Struct. **188**, 377 (1989), and references therein.

[88] S. W. Koch, C. Sieh, T. Meier, F. Jahnke, A. Knorr, P. Brick, M. Hübner, C. Ell, J. Prineas, G. Khitrova, and H. M. Gibbs, J. Lumin. **83/84**, 1 (1999).

[89] M. M. Dignam and M. Hawton, Phys. Rev. B **67**, 035329 (2003).

[90] T. Zhang, X. Li, S. T. Cundiff, R. P. Mirin, and I. Kuznetsova, in *Ultrafast Phenomena XV*, edited by R. J. D. Miller, A. M. Weiner, P. Corkum, and D. M. Jonas (Springer-Verlag, Berlin, 2006).

[91] A. Ishizaki and Y. Tanimura, J. Chem. Phys. **123**, 014503 (2005).

[92] Lijun Yang and M. M. Dignam, Phys. Rev. B **73**, 035334 (2006).